9950-202

DOE/JPL 954355-79/10
Distribution Category UC-63

Mobil Tyco Solar Energy Corporation
16 Hickory Drive
Waltham, Massachusetts 02154

LARGE AREA SILICON SHEET BY EFG

Program Manager: F.V. Wald

Second Quarterly Report - Subcontract No. 954355

(NASA-CR-162597) LARGE AREA SILICON SHEET BY EFG Quarterly Report, 1 Apr. - 30 Jun. 1979 (Mobil Tyco Solar Energy Corp.) 96 p

N80-70373

Unclas
00/44 46084

Covering Period: April 1, 1979 - June 30, 1979

July 15, 1979

"The JPL Low-Cost Silicon Solar Array Project is sponsored by the Department of Energy and forms part of the Solar Photovoltaic Conversion Program to initiate a major effort toward the development of low-cost solar arrays. This work was performed for the Jet Propulsion Laboratory, California Institute of Technology by agreement between NASA and DOE."

ABSTRACT

In Furnace No. 1 during this quarter, experiments were conducted in which the total argon purge rate in this furnace was decreased. A number of extremely significant changes in the crystallographic structure and electronic quality of the ribbons were observed in these experiments. Ribbon segments were grown in which the "equilibrium defect structure" was no longer present and the electrical properties improved to the extent that cells of 50 cm^2 area having AM1 efficiencies over 11% could be prepared.

In Furnace No. 3A, the final five-ribbon demonstration run was performed. The furnace performed nearly flawlessly over the 15 hour run during which ~30 meters of 5 cm wide ribbon were grown at a rate of ~3.3 cm/min from each of the five cartridges. Initial evaluation of a small lot of 45 cm^2 solar cells revealed that the material was capable of being processed into cells of ~9% (AM1) efficiency.

Subsequent to this final multiple demonstration run, the furnace was converted to be operated with three 10 cm width cartridges, plus a melt replenishment unit. This conversion is now complete, and the first growth runs using one cartridge and the melt replenisher have produced ~4 meters of 10 cm wide ribbon at a growth rate of 3.5 cm/min.

In Furnace 17, work on stress has continued, and a basic investigation of stress and buckle generation in the ribbon has shown this to be a fairly complex problem at high growth rates. However, at rates up to perhaps 5 cm/min, the problem may be manageable through improvements in puller design and ribbon guidance. Also on this machine, the work with automatic control designs is making progress, and in an appendix to this report, a very comprehensive discussion of the control dynamics during EFG growth is provided.

"This report was prepared as an account of work sponsored by the United States Government. Neither the United States nor the United States Department of Energy, nor any of their employees, nor any of their contractors, subcontractors, or their employees, makes any warranty express or implied, or assumes any legal liability or responsibility for the accuracy, completeness or usefulness of any information, apparatus, product or process disclosed, or represents that its use would not infringe privately owned rights."

PAGE ii INTENTIONALLY BLANK

Table of Contents

SECTION		PAGE
	ABSTRACT	iii
I.	INTRODUCTION	1
II.	WORK ON CRYSTAL GROWTH STATION NO. 1	5
	A. Overview	5
	B. Experimental	5
	C. Material Quality Considerations	13
III.	MULTIPLE FURNACE	15
	A. Overview	15
	B. Ribbon Growth Activity Summary	16
	C. Silicon Carbide Particle Problem	16
	D. Long Growth Run 184	19
	E. Multiple Growth Runs 185 and 187	22
	F. 10 cm Ribbon Growth Development	26
	G. Acknowledgements	29
IV.	CELL AND MATERIALS CHARACTERIZATION	31
	A. Cell Characterization and Methods Development	31
	B. Materials Characterization	45
	C. Microscopic Crystallographic and Chemical Studies on Ribbons from the "Gas Flow" Experiments	51
V.	MACHINE 17	59
	A. Overview	59
	B. Experimental Studies and Conclusions on Stress in Ribbons	59
	REFERENCES	63
	APPENDICES	65

PAGE iv INTENTIONALLY BLANK

List of Figures

FIGURE		PAGE
1	Meniscus and interface region appearance during steady-state growth	12
2	Silicon carbide particle count per 5 x 10 cm ribbon segment	21
3	10 cm wide ribbon emerging from the top of Furnace 3A during recent startup runs with the first 10 cm width cartridge	28
4	The standard 5 x 10 cm^2 solar cell configuration used to evaluate material grown in both Furnace No. 1 and No. 3A	32
5	Empirical result of fill factor as a function of the voltage and current probe spacing on two commercial CZ cells	41
6	"Worst case" calculation for the percentage change of fill factor, ΔFF, as a function of the probe spacing and bus bar resistance in a typical 10 cm x 5 cm ribbon cell	43
7	Calculated efficiency loss due to the series resistance in the measurement setup	44
8	Minority carrier diffusion length (sample average) vs. time for run 16-184	49
9	Four-point resistivity vs. time, five-ribbon run 16-185 (second half of run only)	50
10	L_D vs. time, five-ribbon run 16-185 (second half of run only)	52
11	Silicon carbide particle surface density vs. time, five-cartridge run 16-185 (second half of run only)	53
12	Sample average diffusion lengths for multiple growth run 16-187	54
13	Photomicrographs of heavy film which appears on silicon ribbon grown with very much reduced gas flow	55
14	Cross sections of silicon ribbon which have been syton-polished and etched in the Sirtl etchant	57
15	Surface structure of ribbon segments etched in 30% KOH solution to remove surface film and reveal grain structure	58

List of Tables

TABLE		PAGE
I	JPL No. 1 Run Data	6
II	JPL No. 3A: Last Series of Growth Runs with 5 cm Width Cartridges	17
III	Silicon Carbide Particle Densities, Run 16-185	20
IV	Silicon Carbide Particle Densities, Run 16-187	20
V	Furnace 3A Multiple Growth Demonstration Run No. 185	23
VI	Furnace 3A Multiple Growth Demonstration Run No. 187	24
VII	Contribution of Various Metallization Loss Mechanisms to Decreased Solar Cell Performance in Large Area Cells	33
VIII	Summary of Solar Cell Data for Ribbons Grown from Furnace No. 3A	35
IX	Summary of Solar Cell Data for Ribbons Grown from Furnace No. 1	37
X	Summary of Solar Cell Data for Ribbons Grown from Furnace 18 During Recent Ambient Gas Experiments	39
XI	Minority Carrier Diffusion Length Averages for Runs done in JPL No. 1	46
XII	Examples of Diffusion Length Variations During Runs with Main Zone Argon Purge Rate Experimentation	48

I. INTRODUCTION

At the beginning of the fiscal year on which this document reports, it was well established that EFG material, in spite of its imperfect nature, is quite capable of producing large area (2.5 x 10 cm^2) solar cells with efficiencies of at least 12%. Indeed, the discussion of whether small area cells of higher efficiency could conceivably be prepared from some of the material, had already been shifting to the question of defining the influence of particular defects on the overall yield of cells prepared from whole multiple meter lengths of ribbon, and attempts to prepare single cells with optimized properties were de-emphasized.

Instead, under this contract the focus shifted to considering even larger cells (5 x 10 cm^2 and 7.5 x 7.5 cm^2) prepared from 5 cm and 7.5 cm wide ribbon, grown under conditions which would make high rate multiple ribbon growth a practical reality. The characterization task, therefore, took more and more of an interest in questions related to uniformity of properties over very large cell areas and within long ribbons, instead of concerning itself with the top performance of selected small ribbon areas.

Thus, the program in its philosophy shifted to engineering research, i.e., answering questions related to specific machine design elements; the ribbon quality to be expected from growth stations built in certain ways and using particular materials of construction, and the relations between silicon ribbon quality and productivity; i.e., such questions as to how speed and width affect the ribbon properties both from a mechanical (flatness, thickness uniformity, etc.) and solid-state (in the end, solar cell efficiency) standpoint.

Overall, we believe that this programmatic approach has been successful and that a realistic engineering concept has been proven which will allow the achievement of high ribbon productivity along with good ribbon quality and thus low solar cell blank cost. Specifically, major achieve-

ments of the program which support this statement are:

1. The soundness of the engineering concepts has been demonstrated by the achievement of multiple (five) ribbon growth for periods up to 20 hours.

2. Significantly improved single ribbon equipment using a cartridge (Machine 17) has been constructed on schedule this year. It provides unique capabilities for studying and understanding the growth process itself as well as a simple basic concept for automatic feedback control.

3. The work on JPL Machine No. 1 (MTSEC No. 18) has led to the design of highly reliable growth cartridges in which experiments of 7.5 cm wide growth can be conducted in a reproducible manner, i.e., when one sets out to grow a ribbon, one can actually grow as much as a full crucible allows every time. During the last three months, this equipment operated on a regular schedule of two one-day runs per week, without any significant parts failure.

4. The introduction of the so-called "mini cold shoe" represents a major advance in reliable cartridge design.

5. A concept that had been proposed for some time, namely to use specific interface shaping to improve material properties of wide ribbon, has finally been reduced to practicability by the use of displaced dies. This has led to solar cells (in sizes of 2.5 x 10 cm^2, 2.5 x 7.5 cm^2, and 7.5 x 7.5 cm^2) grown from a reliable, practical cartridge system which have average efficiencies of over 9% in random lots of ~10 pieces. Most importantly, the material is indeed asymmetrical as predicted, not only with respect to solar cell efficiency but also with respect to silicon carbide density.

Thus, enough understanding of the effects has been gained to make further advances in this area quite likely so that the solar cell efficiency in these large ribbon cells is expected to reach similar averages which are now obtained in cells made from smaller ribbons.

6. Detailed studies of the effect of the gaseous environment in an EFG furnace have led to the discovery that growth stability can be significantly enhanced and SiC density can be greatly reduced by proper atmosphere control.

However, before final production machine prototype design can begin, the various approaches which have been derived need still to be optimized and made ready for fully automatic operation at high growth rates, a fact

that becomes clearly apparent from the detailed discussions in the text that follows. In particular, the main hurdle toward higher growth rates, namely the buckling that produces unacceptable, non-flat ribbon, has to be overcome and the approaches toward higher cell efficiencies have to be refined so that they are more effective and can be combined with high growth rates (> 5 cm/min).

Experiments which generate the needed basic facts in these areas can, however, be conducted now in an optimum way, since both direct observational tools (Machine 17) and sufficient basic understanding of the details of the growth process are available. We are thus confident that the final prototype design of a ribbon production machine could begin within a year.

II. WORK ON CRYSTAL GROWTH STATION NO. 1 by J.P. Kalejs

A. Overview

Significant improvements in as-grown material quality and in solar cell performance have been observed for ribbon growth during this quarter. These have accompanied experimentation with the ribbon growth interface ambient through variation of argon purge rates in the furnace and cartridge. Deviations from the equilibrium defect structure characteristic of EFG ribbon have been associated with these ambient changes, and these are taken to indicate that important changes have taken place in the growth interface region as a consequence. The quality improvements have led to large area (~50 cm^2) ribbon cells with AM1 efficiencies as high as 11.5% (AR coated). These preliminary experiments with the furnace ambient hold out promise that this may be a useful means by which to control certain aspects of the ribbon growth process in a way that could be beneficial in improving material quality still further.

Investigation of growth with radiused displaced dies was initiated concurrently with the furnace ambient studies. Growth conditions with dies having both uniform and nonuniform die-top flat widths have been found to be acceptable.

B. Experimental

The third series of clean runs was completed with two runs this quarter and a fourth series started after a thorough cleaning and rebuilding of the JPL No. 1 growth system. The run data are summarized in Table I. The growth system utilizing all-graphite main zone insulation, graphite die-top shield, and no cold shoe had proven to allow reasonable growth in the speed range from 1.5 to 2.5 cm/min. It was selected for use in continuing quality experiments in order to establish a more extensive statistical data base using an operational mode which would approach that of growth at 2.5 cm width in RF powered furnaces more

PAGE 4 INTENTIONALLY BLANK

Table I. JPL No. 1 Run Data. All Runs with Graphite Main Zone Insulation and without Cold Shoe, Except as Noted.

Run No.	Speed (cm/sec)	Length (m)	Die Type*	Comments**
18-137	1.8 - 2.0	3.0	0.050/0.012D/F	Poor growth conditions, high incidence of SiC attributed to water leak in cartridge.
18-138	2.0 - 3.8	1.0	0.025/.008D/F	Last run in third clean series. All-molybdenum cold shoe. Puller malfunction results in early termination of run.
18-139	-	-	0.050/0.012D/F	Broken afterheater; no growth possible.
18-140	1.7 - 2.0	4.5	0.050/0.012D/F	First run in fourth clean series. Testing of ribbon gas lock and main zone purge rate combinations.
18-141	1.8 - 2.0	2.1	0.025/0.008D/127R	Malfunction of main zone thermocouple limited growth. Constant main zone purge rate. 127 cm radius displaced die with nonuniform die-top flat width.
18-142	1.8 - 2.3	4.5	0.025/0.008D/F	Constant main zone purge rate; good growth conditions.
18-143	1.4 - 2.0	5.1	0.025/0.008D/F	Experimentation with main zone gas purge rate.
18-144	1.8 - 2.5	5.0	0.025/0.008D/63.5R	First test of 63.5 cm radius displaced die with nonuniform die-top flat width. Constant main zone purge rate.

*The first number is the die-top slot width, the second number is the displacement, both in cm. The last designation refers to a flat die (F) or a radius die (R) with the radius given in cm.

**The experiments at constant main zone purge rate used a rate of 10 ℓ/min, which was found to be sufficient to produce a very shiny, film-free ribbon surface typical of the baseline JPL No. 1 material obtained in earlier clean series.

Continued.....

Table I. (Continued).

Run No.	Speed (cm/sec)	Length (m)	Die Type*	Comments**
18-145	1.9 - 2.3	3.8	0.025/0.008D/F	Experimentation with main zone purge rate.
18-146	1.9 - 2.2	4.1	0.025/0.008D/63.5R	Constant main zone gas purge rate. First test of 63.5 cm radius die with uniform die-top flat width.
18-147	1.3 - 1.5	2.2	0.025/0.008D/F	Experimentation with main zone gas purge rate. Severe thermal imbalances at die top limit growth.
18-148	1.5 - 2.0	2.3	0.025/0.012D/F	Experimentation with main zone gas purge rate.
18-149	1.5 - 2.0	2.3	0.025/0.008D/F	Gas purge rate experiments.
18-150	1.5 - 1.9	4.4	0.025/0.008D/127R	Main zone gas off entire run. Gradual film increase on ribbon surface as run progressed.
18-151	1.6 - 1.8	2.4	0.025/0.008D/F	Ribbon splitting, associated with broken after-heater. Main zone purge rate at 2 ℓ/min gives reasonably constant ribbon surface film appearance.
18-152	1.6 - 1.8	0.8	0.025/0/63.5R	Nonuniform die top flats, no displacement. Run length reduced due to block in cartridge water line.
18-153	1.6 - 1.8	3.1	0.025/0/127R	Rebuilt cartridge. Poor growth conditions, heavy film even at standard main zone gas purge rates (5 to 10 ℓ/min), attributed to cartridge water leak.
18-154	1.6 - 1.8	3.0	0.025/0.012D/127R	Poor growth conditions, heavy film. Cartridge water leak terminated growth.

closely than had previously been attempted. The emphasis in these experiments, therefore, was on establishing a more consistent operating procedure and on restricting developmental work which required major changes in system components from run to run (such as cold shoe and materials of construction). In preparation for the fourth series of runs, the furnace and assembly area were thoroughly cleaned and all aluminum cartridge and belt puller components in close proximity to the growth slot and growing ribbon were Teflon®-coated. Assembly procedures for the cartridge and main zone were improved to reduce the extent of handling of the components and the time of their exposure to the room environment. The use of only one cartridge and curtailment of development work which involved extra assembly time and non-standard procedures have aided in this task. The duty cycle, insofar as the time the furnace is at operational temperatures, was increased by a higher run frequency to further reduce the time the growth system components were exposed to the room environment.

Studies of furnace ambient and die design changes on material quality were carried out concurrently during the fourth series of clean runs. Design changes have been introduced to allow improved control over the furnace atmosphere. The chief emphasis was to study means by which to retain growth stability under variable furnace gas purge rates. This study extended to growth with the main zone purge gases turned completely off. Second, alternating with the ambient studies was the testing of growth conditions with radiused displaced dies. The results of these studies are discussed below.

1. Atmosphere Control Studies

Implementation of design changes aimed at improving control over the furnace and cartridge atmosphere, and so aiding understanding of its role in the growth process, was initiated with this series. Prediction of gas flow patterns and their influence on atmospheric composition in the neighborhood of the interface in the conventional operating mode in JPL No. 1 is difficult. Argon purge gas in the cartridge system is introduced both at a point below the main zone heater and insulation as well as in the cartridge itself. Its chief function is to prevent backstreaming of air through the cartridge growth slot and the outside perimeter of the cartridge. This backstreaming has been identified as a possible source of growth instability and as a mechanism for SiC particle generation at the die top.[1] Auxiliary cartridge gas flow (in addition to that used to

supply the cold shoe) was introduced in run 18-90 to assist in controlling backstreaming, as well as to permit operation at lower levels of main zone purge rates. The latter condition was sought for two reasons. First, the main zone is a possible source of impurity-laden gases; in addition, it is necessary to reduce the amount of gas entering into the cartridge from the main zone during growth from quartz crucibles in order to prevent SiO deposition around the die top and on the cold shoe from interfering with growth. Auxiliary cartridge argon purge rates of 5 to 10 ℓ/min, with the gas introduced through two molybdenum tubes extending to the level of the die-top, were found to be sufficient to accomplish this task. This auxiliary cartridge gas purge system is inadequate for the purpose of the furnace atmosphere studies that were contemplated for several reasons. First, the argon purge rate needed to maintain acceptable growth conditions, although reduced by about a factor of two from that necessary with only main zone purging, still implies that considerable flow velocities are imposed on the ambient surrounding the growth interface and ribbon. The exit gas flow path is poorly defined due to the numerous possible exits for the gas from the cartridge (view slots, floor plates, growth slot); hence transients and turbulent flow conditions could be expected to be associated with convective heat transfer within the growth slot environment, with possible undesirable effects on growth conditions. Second, the purge gas is forced over hot furnace components, among them the molybdenum feed tubes, and die top shields and heaters. As a consequence, potential paths for impurity transport via the ambient are still present.

The effect of a more quiescent cartridge and main zone ambient on growth conditions was examined initially. A gas flow configuration was sought that would allow the furnace purge gas to be completely shut off without introducing intolerable backstreaming of air. The first step in this effort, implemented in run 18-140, was the introduction of a gas "lock" at the point of exit of the ribbon from the cartridge growth slot. This lock consisted of a graphite plenum chamber fastened tightly to the cartridge top plate with narrow entrance and exit slots for the ribbon. Gas inlets introduced argon gas to establish an overpressure, which was relieved by the argon exiting around the ribbon. With this gas flow configuration, it was hoped that control of the backstreaming of air could be further removed from the growth interface, while at the same time the purging argon is not forced over hot system components in the furnace interior.

Experimentation with variable argon purge rates was carried out initially to obtain a comparison of growth conditions and ribbon appearance

with those found under a "standard" set of operating conditions (see Table I footnote). The value of this approach was that changes in the furnace ambient due to extraneous causes could be monitored. These could arise from water leaks in the cartridge, or from differing initial furnace conditions, such as could occur if the cartridge and furnace were not in use for a significant time period before a run. The ribbon grown under "standard" baseline conditions was characterized by a very shiny and smooth appearance, with a very low ($\lesssim$ 0.1 particle/cm^2) SiC density on the high meniscus (displaced die flat) face. The SiC particle density on the low meniscus face was generally high ($\gtrsim$ 5 particles/cm^2) but variable, and dependent very much on the meniscus height and die design parameters. The crystallographic structure was dominated by parallel twin boundaries, characteristic of the equilibrium defect structure of EFG ribbon.

A number of significant changes in growth conditions and ribbon appearance were observed with a decrease in the main zone purge rate from the standard baseline operating level. These are summarized below:

1. At main zone purge rates below about 4 ℓ/min, the ribbon lost its shiny surface appearance as the film began to appear. The film continued to become heavier during operation with lower or zero purge rates, and it did not appear to reach steady-state levels over periods of two to three hours. Instead, the film deposits on the meniscus and die top generally built up to levels which seriously hampered growth. However, restoration of the main zone purge rate to levels of 10 ℓ/min was generally sufficient to eliminate the film and regain a clean ribbon surface. On several occasions, the die top contour was sufficiently modified by these deposits to result in very poor growth after the purge rate was restored to its standard rate. These poor growth conditions were generally associated with heavy SiC particle pick-up on both ribbon faces.

2. During the same time span that the surface film began to appear, the density of visible SiC particles growing at the die top (and also being picked up by the ribbon) decreased; in the intermediate stages of moderate film, SiC particle appearance had decreased noticeably to well below the average levels occurring earlier, and practically disappeared even from the face of the ribbon growing from above the high side of the displaced die. In effect, moderate to heavy film cover was usually accompanied by a significant decrease in the SiC particle density. However, in the case of the heavier film appearance, patches of what appeared to be film were frequently picked up from the die top.

3. Growth stability showed a marked improvement with decreasing purge rate during the time a light to moderate film cover was present. The reduction of SiC particle growth and pick-up contributed to this condition. Additional indications that growth conditions at the interface were more homogeneous appeared in the form of smoother interface appearances. Of course, as the film became heavier, growth conditions destabilized as noted above. Two extremes in interface appearance in steady-state growth during light and heavy film formation conditions are illustrated in Fig. 1. The photographs are of the high meniscus (displaced die) side of the ribbon (with the meniscus as the black band) taken through an anamorphic camera system. The black vertical marker in Fig. 1(b) represents a length of 0.025 cm.

4. In a number of runs in which low ($\lesssim$ 4 ℓ/min) or zero purge rates were used, significant deviations from equilibrium defect structure began to appear. These were generally in the form of extended regions of what appeared to be large grained polycrystalline silicon. Grains as wide as 5 mm and extending 10 to 20 cm along the growth direction, though not necessarily with boundaries parallel to it, have been observed (see Section IV).

These experimental observations clearly suggest that important changes are taking place in the growth process with reductions in the main zone argon purge rate. However, steady-state ambient conditions, as evidenced by film appearance on the ribbon, are not readily achievable with the present system ambient control arrangement. This complicates the interpretation of the experimental results. In particular, the cause for the onset of heavier film growth at lower purge rates is not known. The action of reducing the main zone purge rate increases the possibility of air backstreaming even with the gas lock around the ribbon. On the other hand, ongoing processes in the furnace interior (such as component outgassing or small water leaks) also cannot be ruled out as contributing significantly to ambient changes in the growth interface environment.

2. Die Design Studies

Several different die designs have been tested during the course of this series of runs. The purpose of these tests has been to explore growth conditions with displaced radiused dies in conjunction with the studies of the effect of interface shape variations on material structure and quality. The available parameters in this study are the die radius, the width of the die-top slots, and the die displacement.

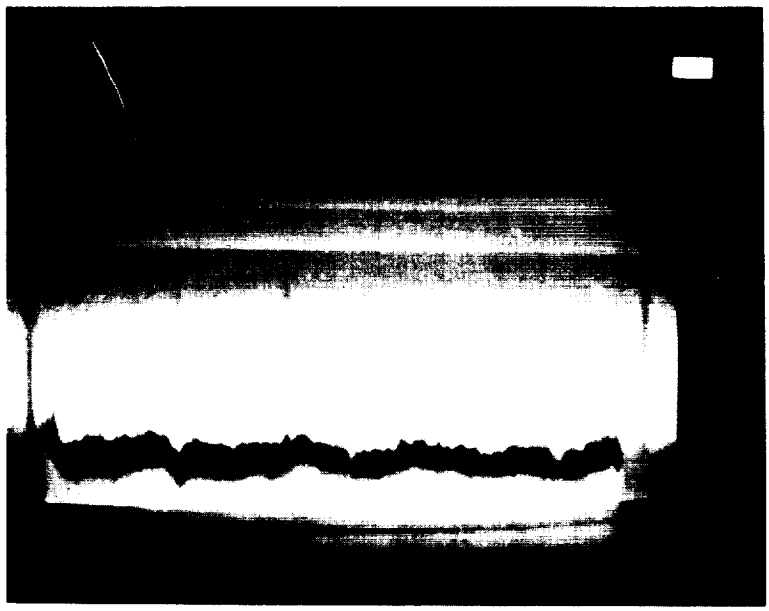

(a)

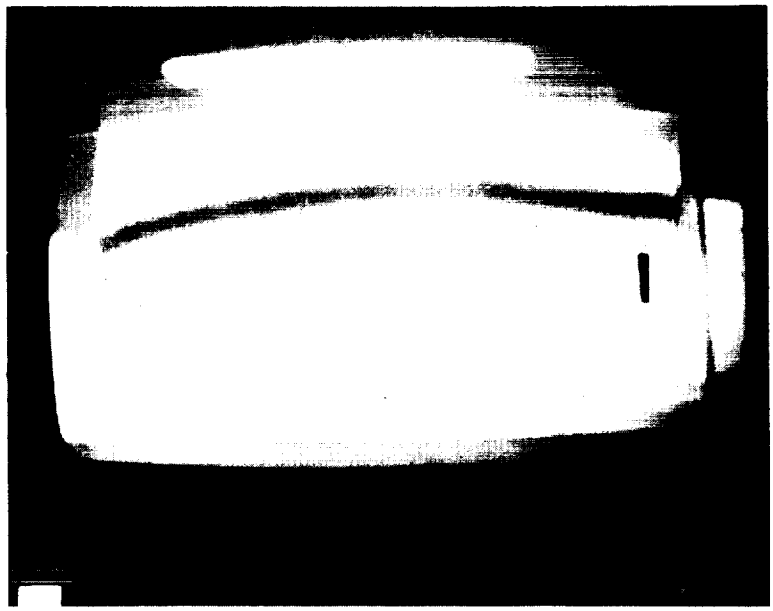

(b)

Fig. 1. Meniscus and interface region appearance during steady-state growth under conditions of (a) light film formation (ribbon 18-151-1), and (b) heavy film formation (ribbon 18-153-3) with reduced main zone argon purge rate.

Radii of 127 cm and 63.5 cm lower the die center relative to the ends by approximately 0.03 cm and 0.07 cm, respectively, over a 5 cm span. In addition, the die flat width can be refinished to be uniform over the width of the die. If it is left unmachined after the cutting of the radius, the flat width will be nonuniform. A displacement of one radi-used flat relative to the other is the final operation. This also creates a nonuniform flat width. Growth conditions with the various die geometries tested were variable but usually reasonable. The ribbon grown will be examined to look for changes in material properties which may arise as a consequence of the change in interface shape across the ribbon width imposed by the radius.

C. Material Quality Considerations

Characterization of as-grown material and data for solar cells made from ribbon growth in the runs of the fourth clean series are discussed in Section IV. Both SPV diffusion lengths and cell performance levels have shown improvements. These are most evident in the new highs for diffusion length and cell efficiencies in the JPL No. 1 growth station achieved with this ribbon: SPV diffusion lengths of over 50 μm over the full width of 5.5 cm wide ribbon, and large area (45 to 55 cm^2) cells with AM1 efficiencies up to ~11.5% (AR coated). Possible reasons for these improvements are discussed below.

The experimental evidence strongly suggests that the ambient change effected as a consequence of main zone purge rate decreases is the most important factor in the increase of ribbon quality in these experiments. Possible growth system responses to such a change can be placed into two categories for the sake of discussion. There are those that relate to improvements in growth stability and contribute to the formation and maintaining of a more homogeneous boundary layer at the growth interface on a local (microscopic) scale. This is evidenced by a more planar and smoother-looking interface, and, as noted above, by the nearly complete absence of SiC particles and pick-up on both ribbon faces. The decrease in the rate of SiC formation could either be the consequence of a lower level of perturbation of the meniscus and boundary layer region, or conversely, itself be responsible for the establishment of a more regular interface during growth. A decrease in the purge gas rate, hence in the gas velocities near the growth interface, could also be expected to reduce the level of thermal perturbations of the interface arising from convection-induced heat transfer irregularities. The net effect of a reduction in interface perturbations through any one or a combination of

these mechanisms could then be very beneficial in improving material quality by affecting both the crystallinity of the ribbon and/or the manner in which impurities are incorporated into it during growth.

On the other hand, the growth system response to purge rate changes may be of a chemical nature. The appearance of the film with decreasing purge rate indicates that the compositional balance in the ambient gases which interact with the ribbon and melt has changed. Part of the film formation is known to take place as a result of ambient gas interaction with the ribbon surface over a region of the order of 1 cm above the growth interface. Evidence for this is in the form of a heavier film region, or "burn" marks, observed on the ribbon at each freeze, which arises when the ribbon is essentially stationary for several minutes until growth is re-started. The intensity of the film layer formed during freezes is clearly a function of the purge rate and the time the ribbon is stationary. In general, in growth with purge rates for which the ribbon surface formed during steady-state growth does not show any visible traces of film, the surface has remained essentially film-free even during freezes. If the film were to be attributed entirely to ambient interactions with the ribbon surface, such as is known to be occurring during freezes, then it could be postulated that the film could influence ribbon quality either through acting as a passivating surface layer which reduces ambient impurity contact with the ribbon or by some process of gettering of impurities within the ribbon. However, in this situation it could be difficult to understand how the film could affect ribbon structure and growth process stability in the manner observed and described above. That these effects are taking place is suggestive of a broader ambient influence, which extends to processes operative within the meniscus and near the growth interface. Changes in the impurity balance in the meniscus, particularly within the impurity boundary layer adjacent to the growth interface, could further influence the rate of incorporation of impurities into the ribbon.

III. MULTIPLE FURNACE 3A by B.H. Mackintosh

A. Overview

Work in the early part of this quarter was concentrated on resolution of two problems identified in the First Quarterly Report as preventing satisfactory five-ribbon operation of this machine. The first of these two problems, namely an inadequate melt replenishment rate, was solved by the design changes which were in the parts-procurement stage at the end of the first quarter. Replenishment performance proved satisfactory in the two long five-ribbon runs subsequently made.

The other problem, high surface silicon carbide particle densities, was further investigated in three single-cartridge runs. The various measurements and observations made led to the tentative conclusion that in this furnace, in its present state, the condition of the surface of the graphite crucible plays a more important role than the composition of the furnace atmosphere in determining the density of these particles on the ribbon surfaces. We found that as long runs with melt replenishment proceed, the density of these particles on the low die-tip side of the ribbons eventually falls to a few per 50 cm^2 "cell blank" segment. We interpret this as an indication that the rate of carbon dissolution from the crucible has slowed to a point where carbon concentration is substantially lower than that in a charge melted in a crucible with a fresh carbon surface. The threshold of three particles per 50 cm^2 cell blank has been somewhat arbitrarily chosen as a density at which silicon carbide particles do not seriously degrade performance of cells at their current level of conversion efficiency as limited by minority carrier diffusion length. The major portion of ribbon grown in this furnace in two runs of this period met this quality criterion for silicon carbide particle density.

Progress in the above two problem areas permitted two highly successful five-ribbon demonstration runs to be made. The second of these

clearly surpassed the 1978 throughput goals for this system, namely five ribbons of 20 meters per run at a duty rate of 70%. A total quantity of 150 meters was grown in 15.5 hours at a duty rate of 94%. The photovoltaic conversion efficiency goal of 9% devices was almost realized, with an actual average cell efficiency of 8.72% in the first (small) batch of devices made from a random selection of pieces.

We consider this demonstration run to accurately represent the current state of development of the 5 x 5 cm ribbon machine. Its design and operation are sufficiently well defined that it could be run on a routine basis at this level of performance. However, the throughput parameters derived from the 1977 SAMICS study of multiple ribbon EFG have been interpreted as requiring the multiple growth of wider ribbon. Thus, as planned, Furnace 3A was converted for development work on the 10 cm growth cartridge at the end of this quarter.

This scaling to 10 cm ribbon made rapid progress. Full-width ribbon was grown in the fourth day's operation of the new cartridge. In the sixth growth run, 3.5 meters of 10+ cm wide ribbon were produced with good flatness, negligible stress, and at comparable pulling rate to the 5 cm ribbon. Experimental work is now being directed to producing clean, carbide-free, and thinner ribbon. Design work is underway to convert the two single-cartridge furnaces JPL No. 1 and No. 17 for use of the 10 cm cartridge as well.

B. Ribbon Growth Activity Summary

Table II summarizes the growth runs performed prior to conversion to the 10 cm cartridge. The first run was intended to provide information to the stress-analysis task of this project and will not be discussed here. Principal results and conclusions from the remaining runs are discussed in the following sections.

C. Silicon Carbide Particle Problem

Within the time frame and other constraints of operating this furnace toward its "5 x 5 cm" demonstration goals, it has not been possible to understand the phenomena controlling silicon carbide particle formation at a fundamental level. Instead, we have experimentally sought changes in component design and operating technique which tend to reduce the severity of the problem. Those measures by which we attempted to affect carbide particle formation by reducing the concentration of reactive gases in the furnace had little effect. The measures used included

Table II. JPL No. 3A: Last Series of Growth Runs with 5 cm Width Cartridges.

Run No.	Purposes	Principal Findings
181	Test cartridge with thin gap between linear cooling plates. Non-displaced die.	Thin gap constrained ribbon buckles. Buckle period decreased. Heavy SiC particle concentrations.
182	Measure $\|CO\|$ in furnace and $\|H_2O\|$ in argon supply. Find purging flow rate giving lowest steady-state $\|CO\|$.	Minimum $\|CO\|$ about 25 ppm with purging flow rate of 32 ℓ/min. Heavy SiC particle concentrations.
183	Wait until $\|CO\|$ levels off at 25 ppm before melting silicon. Conduct entire run with this low concentration.	SiC particle density not lower than in previous run when $\|CO\|$ was several hundred ppm in first hour.
184	Test modified melt replenisher. Operate single cartridge for long period (19 hours continuous growth).	Melt replenisher worked at five-ribbon rate. Results of long growth period represented by Figs. 2 and 8 and Table VIII.
185	Five-ribbon demonstration run.	Total quantity grown: 95 meters at 77 duty rate. Suspected melt contaminations. Refer to Tables III and V and Figs. 9, 10 and 11.
186	Single-cartridge run with used crucible.	Virtually free of SiC on high meniscus side for entire run.
187	Five-ribbon demonstration run.	Total quantity grown: 150 meters at 94% duty rate. Refer to Tables IV, V and VIII and Fig. 12.

vacuum baking the furnace before runs to drive off water vapor, constant monitoring of water vapor level in the argon supply, and "calibration" of the furnace for optimum argon purge rate by measuring CO concentration in the hot zone interior. Non-replenished run 183, made under the optimum attainable condition in these respects showed carbide particle densities in the high-meniscus side (displaced dies were used for all 5 cm growth except run 181) of > 20 per 50 cm^2 area. In contrast to these negative results, the effects of long duration growth with melt replenishment upon carbide particle densities, seen in the next four runs, were beneficial and consistent.

The first occasion on which this effect was identified was the latter half of multiple run 180, as described in the First Quarterly Report. A rather abrupt decrease in carbide particle densities after a period of steady-state growth was again seen in runs 184 and 185. This suggested the simple hypothesis that when silicon is melted in a graphite crucible, it quickly becomes saturated with carbon, but as a run progresses with continuous melt replenishment, the rate of dissolution of carbon slows and the melt's carbon concentration decreases. The location, size, and density of silicon carbide particles on the ribbon are determined by the action of the displaced-tip die. There appear to be threshold conditions below which virtually all carbon which leaves the solution at the growth interface does so by growing into silicon carbon aggregates on the low meniscus side of the die. Above this threshold, the nature of which is not known at present, particle growth occurs on the high-meniscus side as well.

These assumptions about the importance of the carbon dissolution rate at the crucible wall in determining carbide particle formation are substantiated by the outcome of runs 186 and 187. In the first of these, a previously-used crucible was employed without subjecting it to the usual etching and halogen baking. Ribbon grown from this crucible, whose surface already had a stable SiC layer at the outset, was free of carbon particles on the high-meniscus side over its entire length. A different crucible variation was employed in multiple run 187: the surface area in contact with silicon was reduced as much as was practical, by about 1/3 compared with the crucible of similar run 185. Compared with 185, the method of charging the crucible was also different. Instead of precharging the crucible to its capacity, only a sprinkling of silicon chips was placed in the crucible. This silicon was melted and allowed to "soak into" the crucible walls for ½ hour before filling with the melt replen-

isher and commencing growth. Comparison of Tables III and IV shows that carbide particle densities fell to an acceptable level much earlier in run 187. We currently assume that in the long growth runs (e.g., one week) foreseen for EFG production, the worst to be feared is the rejection of the first few meters of material grown because of high carbide particle densities. Future advances in crucible materials, die design, and in understanding furnace chemistry may further reduce the problem.

D. Long Growth Run 184

In its initial trial run, the melt feeding unit was found to work well in its modified form. After a rate of melting into the crucible equivalent to withdrawal of five ribbons was demonstrated, a decision was made to continue the single-cartridge growth for a long period, which turned out to be about 18 hours (39.6 m at 3.6 cm/min). Growth was extremely stable and was continuous during this period, except for one freeze after 13 hours. This long period of steady-state growth with semi-continuous replenishment presented an opportunity to observe the progression of key ribbon characteristics, namely silicon carbide particle density, diffusion length, and resistivity, and to test the longevity of critical components such as die, die heaters, and melting funnel. The observations made on this run are as follows:

1. Silicon Carbide Particle Density

After an initial length of about 2 m of ribbon was grown, silicon carbide particle densities on the high-meniscus side fell to $\leq$ 5 per 50 cm^2. Counts of particles per 50 cm^2 segment were made on subsequent ribbon at 50 cm intervals. The distribution of densities is shown in Fig. 2.

2. Resistivity

Four-point probe resistivity measurements made on this material demonstrate very uniform values over the total length of the run. These measurements are interesting principally insofar as they verify that the quantity of dopant was properly calculated; the intended doping level of 1.0 Ω-cm was accurately maintained. The method of supplying boron dopant to a continuously-replenished crucible is to drill holes into the polysilicon charge rod, using a tungsten carbide glass drill, and to insert "Dope Sil" pellets. The concentration and spacing of the pellets are chosen so that each time about one-fourth the contents of the crucible is withdrawn and replaced, a pellet is added.

Table III. Silicon Carbide Particle Densities, Run 16-185. Percentage of Ribbon from Each Growth Station Meeting the Criteria of $\leq$ 10 and $\leq$ 3 Particles per 50 cm^2.

	Particles per 50 cm^2	
Station No.	$\leq$ 10	$\leq$ 3
1	25%	0
2	33%	25%
3	0	0
4	86%	60%
5	36%	7%

Table IV. Silicon Carbide Particle Densities, Run 16-187. Percentage of Ribbon from Each Growth Station Meeting the Criteria of $\leq$ 10, $\leq$ 5, and $\leq$ 3 Particles per 50 cm^2.

	Particles per 50 cm^2		
Station No.	$\leq$ 10	$\leq$ 5	$\leq$ 3
1	100%	99%	91%
2	98%	93%	83%
3	97%	93%	80%
4	100%	99%	90%
5	86%	78%	68%

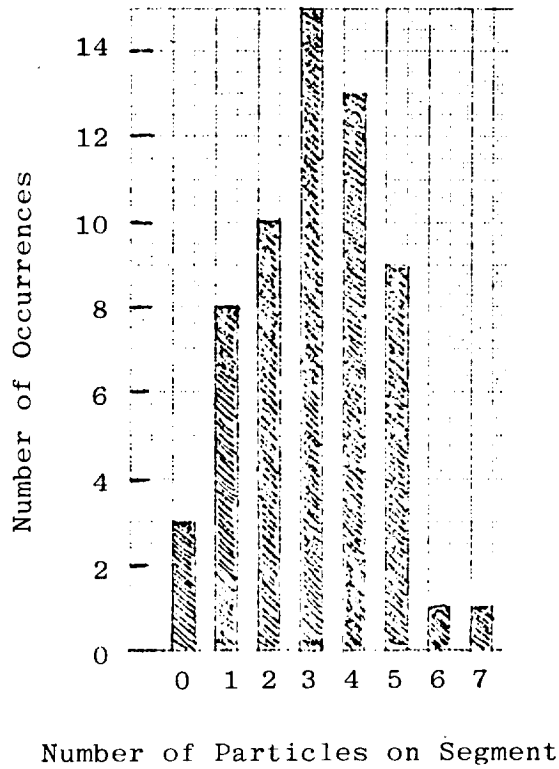

Fig. 2. Silicon carbide particle count per 5 x 10 cm ribbon segment. 15% sampling of run 16-184.

3. Diffusion Length

This run was particularly significant in the opportunity presented to observe the tendency of measured diffusion length to asymptotically approach a steady-state value. If one assumes that there are two types of impurity sources present in the growth system, namely those associated with the beginning of an operating cycle and those which act continuously during running, then one sees that eventually in long steady-state running, the latter type of sources predominate. Examples of impurity sources associated with start-up of a run cycle are dust particles which fall in when the furnace is open for loading and surface contamination of crucible and other parts. Impurity sources which act continuously during the run are those which diffuse out from within various components, gas-borne oxides of metal furnace components, surface contamination of replenishment feed material, and so forth. The diffusion length measurements presented in Fig. 8 (Section IV) suggest an asymptotic approach to the range of 20 to 25 microns, which indicates that there are impurity sources operating continuously in this furnace. The relationships between furnace construction materials, gas flow paths within growth systems, and ribbon electronic quality are currently under investigation in Furnace JPL No. 1. This work will provide guidance in identifying and reducing or eliminating these impurity sources.

4. Longevity of Components

No deterioration of growth stability was observed with passage of time, nor was the functioning of any component impaired. The die bottom was covered with a thick clump of silicon and silicon carbide platelets when withdrawn from the furnace, but these did not apparently degrade growth stability. Dies exposed to silicon for long periods crack up more severely upon cool-down than dies used in shorter runs, but as long as they remain at temperature, their dimensions do not perceptibly change either from warpage or erosion. No repair or replacement of any other cartridge part was necessary following the run.

E. Multiple Growth Runs 185 and 187

These two runs were conducted similarly except for differences in crucible design and charging, and the use of a batch of dies which were more uniformly and accurately machined in the latter run. The throughput-related performance realized in these runs is presented in Tables V and VI. Figures for duty rate are based on the following definition:

Table V. Furnace 3A Multiple Growth Demonstration Run No. 185.

Station No.	1	2	3	4	5
Total Quantity (meters)	21.6	22.0	19.5	11.3	20.7
Total Duration of Growth (minutes)	611	612	588	350	630
Percentage of 12-Hour Run Period* Actually Growing	85	85	82	49	88
Number of Freezes	6	3	8	4	3
Longest Duration of Continuous Growth (minutes)	200	200	220	95	355
Average Growth Rate (cm/minute)	3.53	3.59	3.32	3.22	3.28
Overall Duty Rate	.775				

*See text for definition of run period.

Table VI. Furnace 3A Multiple Growth Demonstration Run No. 187.

Station No.	1	2	3	4	5
Total Quantity (meters)	30.4	29.6	29.9	31.1	27.7
Total Duration of Growth (minutes)	910	890	825	919	829
Percentage of 15.5-Hour Run Period* Actually Growing	97.8	95.7	88.7	98.8	89.1
Number of Freezes	3	5	6	3	4
Longest Duration of Continuous Growth (minutes)	692	331	505	490	508
Average Growth Rate (cm/minute)	3.34	3.33	3.62	3.38	3.34
Overall Duty Rate	.940				

*See text for definition of run period.

The run is defined to begin when the operator begins pulling the first ribbon, and to end when the five growth stations run out of silicon more or less simultaneously following cessation of replenishment. Thus, the duty rate does not account for time taken to load and heat up the furnace, or time taken to insert the cartridges. It does account for loss of production due to initiation of growth of the four ribbons after the first has been started, and losses due to freezes and equipment malfunctions.

In run 185, the greatest single loss of duty rate was the necessity to remove one of the cartridges twice, once for replacement of a mismachined die, and once to repair the effects of a silicon flood. Simultaneous five-ribbon growth was maintained for a total of 180 minutes, or 25% of the run period. No cartridge removal was required in run 187, but one station was unproductive for a half hour when an electrical connection became loose, damaging a cartridge heater transformer. Five ribbons were simultaneously grown during 77% of the run period, including a five hour period spanning midday during which not a single freeze occurred. Numerous freezes occurred between the hours of 5 and 7 p.m., suggesting that the sensitivity of the control systems to power line transients needs to be reduced.

Two problems detracted from the quality of material from run 185. Most ribbon grown in the first half of the run bore concentrations of silicon carbide particles greater than ten per 50 cm^2. These concentrations decreased in monotonic fashion in the second half, and in the case of three cartridges, eventually fell below the threshold of three per 50 cm^2, as seen in Table III.

A second quality-related problem showed up when resistivity measurements were made on the ribbon produced. The resistivity of ribbon from each of the five cartridges was, at the run's beginning, about one-half the 1.0 Ω-cm target resistivity for which the melt was boron doped. This low resistivity, which gradually rose as the run progressed, indicates that the starting charge with which the crucible was filled may have been contaminated. Resistivity and diffusion length measurements for this run are presented in Section IV. No other cases of apparent contamination of the silicon charge have recently occurred in operating this furnace, but foreign matter was found in samples of the type of silicon used in this run shortly afterward.

The silicon carbide particle problem was much reduced in run 187, for reasons already discussed, and over 80% of the "cell blank" segments

produced meet the criterion of fewer than three particles (Table IV). Diffusion length and solar cell parameter measurements made on this material show it to compare favorably with that produced in optimum single cartridge runs. These data are presented in Section IV. A 10% sampling of run 187 consisting of 150 "cell blank" pieces 5 cm by 10 cm was sent to JPL.

The progress made in four multiple ribbon runs this year toward demonstrating operation at a "production-worthy" level of performance may be taken as a sign that in most respects the system is quite reliable and operating procedures are well-defined. With a few detail refinements and additional manpower, the system could now be run on a routine basis, producing over 100,000 cm^2 of silicon per 24-hour period. At a device efficiency of 9%, the corresponding photovoltaic capacity would be ~900 watts per day. An important statistic relating to operation of this machine is the energy-payback time for the sheet growth process, which is about 850 hours of AM1 sunlight. (Power consumption of the furnace and subsystems is 32 kW.) The solar cell efficiency level of 9% is used here, as it has essentially been demonstrated in high-productivity growth, but we are quite confident that current and future progress made toward higher efficiency cells in the work of Furnace JPL No. 1 can be duplicated in multiple production.

F. 10 cm Ribbon Growth Development

Conversion of Furnace 3A for developmental work on the 10 cm cartridge entailed replacement of the top half of the hot zone insulation, the furnace chamber top plate, and substitution of a new cartridge power supply and puller.

In the first two days' operation of the cartridge, its basic mechanical, electrical, and thermal characteristics were checked, including the following items:

- Alignments and fits of parts at operating temperature,
- Matching of power supplies to heating elements,
- Voltage drops in power supply cables and connections,
- Temperature of water-cooled structures during operation (heater block, electrical connectors, cold shoes),
- Temperature profile, and maximum attainable temperature of afterheater/linear cooling structures.

Once the cartridge proved satisfactory in these respects, development of ribbon growth began.

In its initial stages, growth development consists of the creation of proper die-top isotherm shapes for stable, full-width growth and controllability during the starting transient. The cartridge-type growth system permits rapid progress toward correct die-top thermal conditions, principally by mechanically profiling the three die heaters or substituting different ones. A die is used during these early stages which is especially "forgiving" by virtue of its wide top slot and its flat, featureless top (no bulbs or displacement). The shape of the liquid-solid interface formed with a constant-thickness seed, the tendency of ribbon to spread over various portions of the die, and the thickness profile of grown ribbon are used as indicators of isotherm shape.

On the third and fourth days' work with the new cartridge, three modifications were made to the heaters, the last of which permitted controllable spreading to 10.75 cm width. After some special constant-thickness, full-width seeds were grown on the fifth day, a run was made in which over 80% of the 4.3 meters grown was over 10 cm wide. The photograph of Fig. 3 was taken during this run.

The goal of the current development work on Furnace 3A is to achieve 10 cm wide growth which is equivalent or superior to recent 5 cm growth in regard to ribbon thickness, flatness, stability, growth rate, and silicon carbide particle density on the high-meniscus side. To achieve this condition, the following features remain to be integrated into operation of the cartridge:

- Narrower die top (from the current .064 cm down to about .04 cm),
- Bulbous ends or equivalent edge-stabilizing feature on die top,
- Displaced-tip die,
- Use of replenishment system.

The cartridge must also be assembled using halogen-baked graphite parts before ribbon material with photovoltaic properties comparable to recent 5 cm ribbon can be grown.

We plan, by year's end, to outfit Furnace 3A with two additional cartridge systems and demonstrate high duty-rate multiple growth. Within the coming quarter, Furnaces JPL No. 1 and No. 17 will be converted for developmental work on the 10 cm cartridge in the areas of higher growth

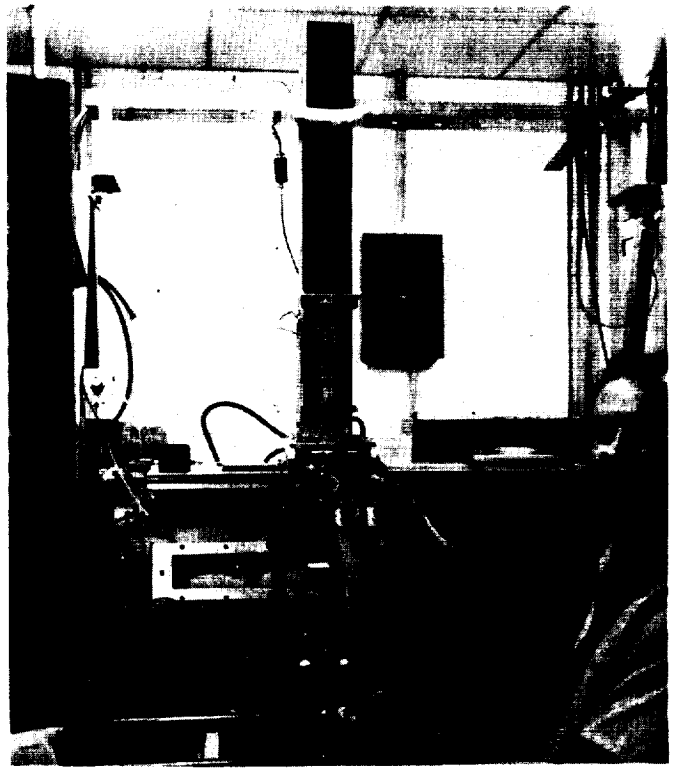

Fig. 3. 10 cm wide ribbon emerging from the top of Furnace 3A during recent startup runs with the first 10 cm width cartridge.

rate, improved electronic quality, and automatic control of growth. Due to the commonality of basic growth systems of all three furnaces, improvements arising from work in one of the single-station developmental furnaces will be more directly applicable to the current multiple furnace and its successor than in the past.

G. Acknowledgements

The author wishes to recognize the skillful and consistent efforts of Mr. Mert Prince and Mr. Raymond Leonard, operators of Furnace 3A.

The patience and insight of Mr. Prince, as principal ribbon grower since the inception of this machine, underlie the viability which cartridge type EFG systems have attained.

The careful attention to detail by Mr. Leonard in setup procedures has resulted in extremely reliable furnace operation, essential to progress in the past year. He also efficiently performs many less visible but essential functions, including charge material preparation, ribbon cutting, incoming parts inspection, and record keeping.

Finally, the physical endurance required to operate this machine for demonstration runs of up to 15 hours (plus set up time) is considerable, and the endurance of Messrs. Prince and Leonard on these occasions has been admirable.

IV. CELL AND MATERIALS CHARACTERIZATION

A. Cell Characterization and Methods Development by C.T. Ho

1. Introduction

During this quarter, all solar cell fabrication was by the "modified standard" process, which some time ago was shown to be the preferable alternative to the "standard process."[2] The process differs from the standard process only in that it uses a CVD diffusion step to form the N^+ junction. All other steps are the same as in the standard process.

The standard mask used for the 5 x 10 cm^2 cells has 40 fingers and a bus bar along one of the long sides (Fig. 4). It is obvious, then, that a compromise must be sought in terms of finger/bus bar resistance vs. metal coverage. The general principles of how we arrived at the current optimization have been published previously.[3] Table VII shows the comparison of the loss factors associated with the grid design for the 2.5 x 10 cm^2 (nominal) cell and the 5 x 10 cm^2 (nominal) cell. As can be seen, the grid design for the larger cell compromises in terms of resistance in order to keep shadowing losses of the metallization low. Actual measurements on the grids, however, revealed an increased resistance of the metallization over the design, and, particularly, an increased and variable metal coverage, which is probably due to the fact that the large cell blanks are not perfectly flat. The metal masks are, therefore, spaced above the silicon piece over wide areas which causes spreading of the metal fingers. Also, on inspection, the masks were found to be no longer in perfect condition and a new set of masks has to be ordered.

Under these circumstances, solar cells fabricated from material grown in the multiple growth system are obtained with an average conversion efficiency of ~9%. From material grown in Station 1, large area

PAGE 30 INTENTIONALLY BLANK

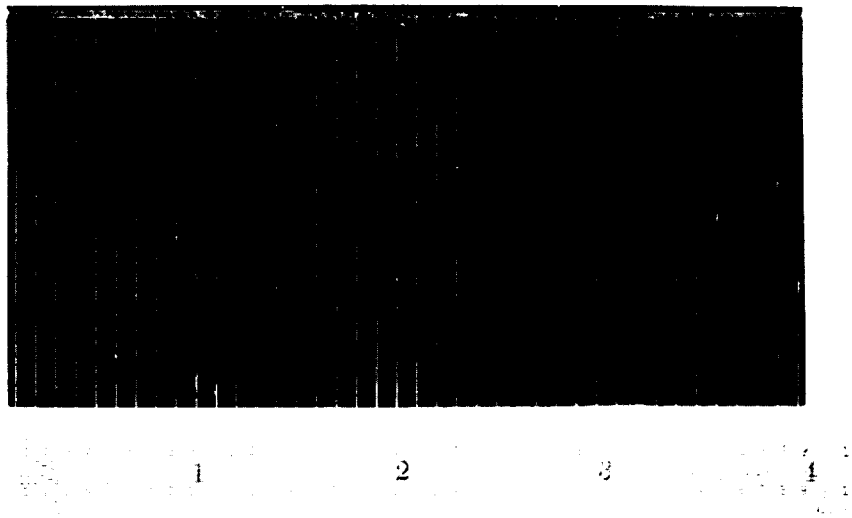

Fig. 4. The standard 5 x 10 cm^2 solar cell configuration used to evaluate material grown in both Furnace No. 1 and No. 3A.

Table VII. Contribution of Various Metallization Loss Mechanisms to Decreased Solar Cell Performance in Large Area Cells.

	Design				Actual	
	$2.5 \times 10\ cm^2$		$5 \times 10\ cm^2$		$5 \times 10\ cm^2$	
Loss Mechanism	(mW)	(%)	(mW)	(%)	(mW)	(%)
Finger Resistivity	0.6	0.3	6.6	1.3	13.2	2.6
Bus Bar Resistivity	0.2	0.1	1.0	0.2	6.0	1.2
Shadowing	24.0	10.9	43.5	8.7	~70	~14.0

($57.7\ cm^2$) cells with efficiencies over 11% have been achieved. These results are described in more detail below.

2. Multiple Growth Furnace

Two solar cell fabrication runs for the ribbons grown from the multiple growth furnace have been completed. The first was made with material from test run 16-184, a single-cartridge run which lasted a total of 18 hours. The second batch of cells was prepared from the demonstration run 16-187, in which ribbons were grown from five cartridges simultaneously under continuous melt replenishment.

The solar cell output data under AM1 simulation measurements are summarized in Table VIII. Cells from run 16-184 show an average conversion efficiency of 7.28%. The cell properties appear to be limited by the bulk diffusion lengths which were measured as 11 to 14 μm in typical samples. However, the results for the multiple growth run 16-187 show definite improvements in the photovoltaic performance. The bulk diffusion lengths, as discussed, were found to be 17 to 26 μm. The overall conversion efficiency is 8.7% with Cartridge No. 3 producing an average efficiency of 9.1%. Although the numbers of all processed cells are not sufficient statistically to provide a basis for making distinctions about the quality of the ribbon produced by each cartridge, the results clearly demonstrate that high throughput ribbon growth using the multiple growth furnace can at present produce solar cells of about 9% efficiency.

3. Cells from System No. 1

A series of growth experiments have been conducted in the JPL System No. 1. The results for the solar cell evaluation of these experiments can be grouped into the following categories: (a) die capillary and crucible type experiments, and (b) gas ambient experiments.

a. Die Capillary and Crucible Type Experiments

In these experiments, the die capillary design (central capillary, saw cut, and central open channel) and the crucible type (quartz and graphite) were chosen as the experimental variables. All the runs were made with displaced dies except run 119. The solar cell performance data, including the growth parameters, for the completed runs are shown in Table IX. Cell conversion efficiencies for the various growth runs fluctuate between 5.6 and 6.2% (not AR coated), or 8.1 to 9.0% if AR coated. In run 18-133, the photovoltaic parameters in J_{sc},

Table VIII. Summary of Solar Cell Data for Ribbons Grown from Furnace No. 3A. All Cell Area = 44.1 cm^2 and AR Coated. ELH Light 100 mW/cm^2. 28°C.

Cell No.	J_{sc} (mA/cm^2)	V_{oc} (Volt)	FF	η (%)	Notes
184-1	21.36	0.526	0.634	7.13	
-2	22.35	0.523	0.625	7.30	
-3	21.92	0.523	0.643	7.36	
-4	21.93	0.525	0.682	7.85	
-5	18.99	0.491	0.645	6.01	
-6	23.43	0.523	0.630	7.71	
-7	21.73	0.518	0.621	6.98	
-8	22.28	0.514	0.611	6.99	
-9	22.29	0.516	0.621	7.14	
-10	21.89	0.515	0.628	7.08	Single Cartridge Run
-11	22.34	0.520	0.633	7.35	
-12	21.53	0.512	0.629	6.93	
-13	22.02	0.525	0.608	7.02	
-14	21.99	0.522	0.599	6.88	
-15	21.43	0.520	0.628	6.99	
-16	22.50	0.523	0.611	7.19	
-17	22.68	0.526	0.686	8.18	
-18	22.39	0.524	0.660	7.75	
-19	21.57	0.514	0.645	7.15	
-20	23.46	0.533	0.682	8.52	
Average	22.0	0.520	0.636	7.28	

Continued ...

Table VIII. (Continued).

Cell No.	J_{sc} (mA/cm^2)	V_{oc} (Volt)	FF	η (%)	Notes
187-1-1	23.30	0.527	0.699	8.63	
-2	23.20	0.531	0.695	8.56	
-3	22.79	0.531	0.673	8.15	
-4	23.26	0.536	0.687	8.56	
-5	24.43	0.545	0.713	9.49	Cartridge No. 1
-6	22.97	0.534	0.730	8.96	
-7	23.00	0.538	0.718	8.89	
-8	23.75	0.533	0.651	8.24	
-9	23.18	0.532	0.700	8.63	
Average	23.32	0.534	0.696	8.68	
187-3-1	23.37	0.531	0.731	9.06	
-2	23.89	0.536	0.705	9.03	
-3	23.67	0.541	0.711	9.12	Cartridge No. 3
-4	23.90	0.535	0.694	8.86	
-5	23.14	0.542	0.729	9.54	
Average	23.79	0.537	0.714	9.12	
187-4-1	22.64	0.523	0.689	8.15	
-2	23.14	0.528	0.684	8.37	
-3	23.54	0.530	0.701	8.74	
-4	22.77	0.534	0.736	8.96	Cartridge No. 4
-5	23.39	0.526	0.665	8.19	
-6	22.74	0.529	0.716	8.62	
-7	23.41	0.536	0.706	8.86	
-8	22.56	0.536	0.706	8.53	
Average	23.02	0.530	0.70	8.55	
187-5-1	23.74	0.534	0.672	8.52	Cartridge No. 5

Table IX. Summary of Solar Cell Data for Ribbons Grown from Furnace No. 1. All Cell Areas ≈ 45 cm^2. ELH Light 100 mW/cm^2. 28°C.

Cell No.	Growth Conditions	J_{sc} (mA/cm^2)	V_{oc} (Volt)	FF	η (%)	$\bar{L}_n$ (μm)	Note
18-117-1	Graphite Crucible	18.04	.530	.686	6.56	26	No AR Coating
-2	Displaced Die	17.04	.515	.612	5.37		
-3	Central Channel	17.70	.506	.694	6.22		
Average		17.59	.517	.664	6.05		
18-118-1	Graphite Crucible	17.70	.523	.681	6.30	25	
-2	Displaced Die	17.31	.520	.638	5.74		
-3	Central Channel	17.59	.530	.70	6.52		
Average		17.53	.524	.673	6.19		
18-119-1	Graphite Crucible	17.92	.521	.633	5.91	19	
-2	Flat Die Central Channel	15.93	.512	.650	5.30		
Average		16.93	.517	.642	5.61		
18-121-1	Graphite Crucible	17.50	.503	.651	5.73	22	
-2	Displaced Die	16.74	.501	.686	5.76		
-3	Open Channel	15.24	.496	.710	5.37		
-4		17.74	.510	.662	6.00		
Average		16.81	.503	.677	5.72		
18-123-1	Quartz Crucible	15.95	.524	.664	5.55	24	
-2	Displaced Die	17.34	.506	.550	4.83		
-3	Open Channel	17.34	.526	.633	5.77		
-4		17.97	.531	.669	6.38		
Average		17.15	.522	.629	5.63		
18-125-1	Graphite Crucible	18.81	.501	.683	6.43	26	
-2	Displaced Die	16.48	.525	.666	5.76		
-3	Open Channel	17.56	.492	.644	5.56		
Average		17.62	.506	.664	5.92		
18-126-1	Quartz Crucible	16.79	.522	.642	5.63	24	
-2	Displaced Die	18.07	.531	.674	6.47		
-3	Open Channel	17.46	.531	.683	6.33		
Average		17.44	.528	.666	6.14		
18-133-1	Graphite Crucible	26.92	.552	.646	9.61	32	AR Coated
-2	Displaced Die	26.08	.549	.651	9.32		
-3	Open Channel	26.97	.551	.650	9.65		
-4		26.01	.545	.606	8.58		
Average		26.50	.549	.638	9.29		

V_{oc}, and L_n were distinctively higher than the other runs. It is not certain, though, which growth parameters of that run are responsible for the favorable results, because both runs 121 and 125 used similar growth conditions with far less favorable results in terms of solar cell outputs. Thus, a definite optimum choice of die design or crucible type to improve the ribbon quality could not be established in these experiments.

b. Ambient Gas Experiments

Several experimental growth runs (143 through 150) have been made with the ambient carrier gas either reduced or completely shut off during the growth (see Section I for details). Ribbon samples from runs 143, 148 and 150 were selected and processed into solar cells. In Table X the solar cells fabricated from these three runs are numbered in ascending order as the ambient gas flow was gradually reduced. For run 143, there is a clear trend in terms of improved photovoltaic properties when the carrier gas flow is diminishing. In runs 148 and 150, the trend was not so well defined. However, the significant result of these experiments is that cell conversion efficiencies around 11% have now been realized in very large area EFG cells, although the mechanisms by which this "gas flow" phenomenon affects the electronic properties of the ribbon are still quite unknown at this time.

4. Influence of Measurement Method on Cell Efficiency

Some time ago, Mobil Tyco adopted a policy to obtain efficiency measurements on its 2.5 x 10 cm^2 cells by using six equally spaced probes along the bus bar. These probes were short-circuited externally to the bus bar and served as simultaneous current and voltage sensors.

This measurement technique, which is contrary to the rest of the industry but is felt to be more conservative (because it is likely to produce lower numerical results for the fill factors), was adopted for two reasons.

Firstly, we felt that such a measurement would more closely approximate the situation which is obtained when single cells are interconnected into strings, i.e., by including some probe resistances into the measurement circuit, one might approximate resistances which would be introduced into a cell string by the interconnecting straps.

Secondly, it was found that for cells with significant bus bar resistance, the fill factor can depend on the distance between the current and voltage probes, if these are kept separate, as in the standard measure-

Table X. Summary of Solar Cell Data for Ribbons Grown from Furnace 18 During Recent Ambient Gas Experiments. Cells are Nominally 5 cm x 10 cm, Areas in cm^2 are Given in Table. Processed Using Hybrid Process. AR Coated.

Cell No.	Area (cm^2)	I_{rv} (mA/cm^2)	V_{oc} (V)	I_p (mA)	I_{sc} (mA/cm^2)	FF	P (mW/cm^2)
143-2	44.48	0.166	0.548	888.2	22.38	0.741	9.10
-4	44.48	0.203	0.552	969.8	24.00	0.751	9.94
-5	44.48	0.535	0.550	1041.9	25.54	0.763	10.72
-7	44.48	0.350	0.561	1082.9	26.19	0.778	11.43
148-3	44.48	0.203	0.555	1010.5	25.74	0.750	10.72
-4	44.48	0.147	0.553	1030.5	24.88	0.792	10.91
-5	44.48	0.147	0.549	1035.1	25.21	0.762	10.54
-5	44.48	0.004	0.556	1066.3	25.77	0.778	11.15
-6	44.48	0.004	0.556	1078.3	25.85	0.781	11.21
150-1	57.71	0.753	0.559	1342.3	25.94	0.731	10.59
-2	57.71	2.330	0.553	1158.0	23.30	0.705	9.08
-3	57.71	1.023	0.569	1334.4	26.27	0.712	10.63
-4	46.73	0.281	0.565	1131.1	27.36	0.744	11.49
-5	46.90	0.472	0.561	1117.7	26.68	0.712	10.65
-6	57.71	0.298	0.564	1298.6	25.64	0.730	10.54
-7	57.71	0.398	0.570	1374.9	26.13	0.744	11.07
-8	57.71	0.469	0.565	1383.1	26.99	0.707	10.79
-9	57.71	0.824	0.566	1369.4	26.39	0.716	10.68
-10	57.71	1.577	0.568	1297.5	26.51	0.704	10.60
-11	57.71	0.426	0.570	1382.7	26.51	0.746	11.28
-12	57.71	1.876	0.564	1230.8	24.95	0.700	9.84
-13	57.71	1.165	0.563	1270.7	25.72	0.715	10.35
-14	57.71	0.455	0.558	1350.0	25.92	0.729	10.54
-15	57.71	0.199	0.558	1198.0	25.34	0.648	9.16

ments. As an example, in Fig. 5 measurement results are shown for the fill factor as a function of the voltage and current probe spacing for two commercial 6 x 2 cm^2 CZ solar cells using two connection schemes, i.e., the current probes are either separated or shorted together. It is clearly indicated that in this case, with the two probes separated, the measured FF increases as much as ~10% for large probe spacings. However, the bus bar resistance in this case also is rather high.

From an analytic point of view, the problem can be seen to be due to the incremental voltage drop along the bus bar which is

$$\frac{dV(X)}{dX} = \rho I(X),$$

where ρ is the resistance per linear length of the bus bar. Since the collected photocurrent, I(X), is also position dependent, the above equation can be expressed in terms of the photovoltaic current, $I_p(X)$,

$$\frac{d^2V(X)}{dX^2} = \rho W I_p(X) = \rho W \left[I_{sc} - I_o \left(e^{\frac{qV(X)}{kT}} - 1 \right) \right].$$

W = cell width,
I_{sc} = cell short circuit current,
I_o = cell dark reverse current.

Then, the voltage-current relation as a function of position could be determined exactly by solving the above equation numerically.

However, let us consider a <u>worst case</u> situation, in which we assume for simplicity that the maximum collected current flowing along the bus bar is the total cell short circuit current, or $I_{pmax} \approx I_{sc}$. The solution of the above equation can then be much simplified:

$$V(X) = \tfrac{1}{2}\rho W I_{sc} X^2 + V_o,$$

$$\text{or} \quad \Delta V(X) = \tfrac{1}{2}\rho W I_{sc} X^2.$$

Finally, the increment of fill factor, FF, as a function of position for this "worst case" can be approximated as

$$\Delta(FF) \approx \frac{\Delta V(X)}{V_{oc}} = \tfrac{1}{2}\rho W \left(\frac{I_{sc}}{V_{oc}}\right) X^2.$$

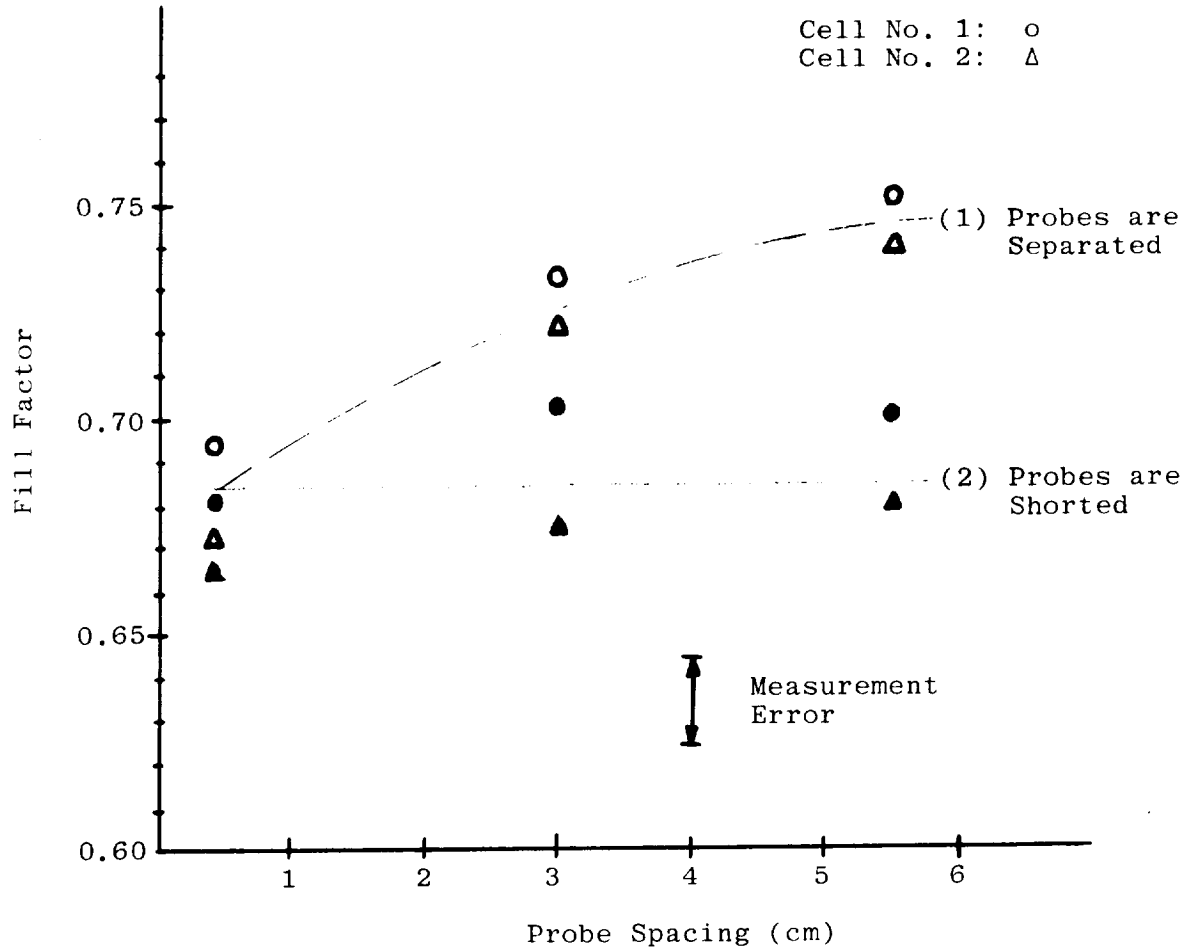

Fig. 5. Empirical result of fill factor as a function of the voltage and current probe spacing on two commercial CZ cells. The measurement was made with two connection schemes: (1) probes are separated, and (2) probes are shorted. The cell size is 6 cm x 2 cm with the bus bar resistance ≈ 0.04 Ω/cm.

For a typical 5 x 10 cm^2 ribbon cell under AM1 conditions ($I_{sc} \approx 1.3$ amps, $V_{oc} \approx 0.55$ V, and W = 5 cm), we plot the calculated percentage increase in FF as a function of probe spacing for a worst case situation, as shown in Fig. 6. In our solar simulation measurement setup, the spacing between the current collector probes and the voltage sensing probe is 1.5 cm. Thus, for the bus bar resistances we usually see in our 5 x 10 cm^2 cells, as indicated by the arrow in Fig. 6, the measured difference between the two probe connection schemes could reach perhaps ~4% for this worst case estimate and the extremes of bus bar resistances.

Thus, when very large area cells are used (such as our present 5 x 10 cm^2 size), measurements with the shorted probes do indeed appear to be unduly conservative since a significant apparent loss of fill factor occurs. This is due to the fact that the series resistance of the probes and wires (up to the shorting point) which connect the bus bar with the measuring circuit is between 0.02 and 0.05 Ω in our measuring system. This resistance is an actual one (i.e., contact resistances are <u>not</u> included yet), while checking to ensure that each probe indeed made proper contact. Under the usual measurement conditions, this is not likely to be always the case, so the losses calculated here are probably minimum. The loss due to the probe resistance is then calculated by introducing a series resistance into a model which includes the distributed nature of an actual solar cell as presented in Ref. (3). Figure 7 presents the general result, and the cross-hatched area indicates the resistance specific to our case. Note that as the cells produce more current (i.e., have higher efficiencies), the slope of these lines would increase and the error would get correspondingly larger. It is clear, then, that for our large area cells, the likelihood of significantly understating the fill factor when measuring with shorted probes is quite high, whereas the danger of overstating it due to excessively large separations and resistances between the voltage and the adjacent current probes is relatively low.

In the future, therefore, we will perform all efficiency measurements with separate current and voltage probes using the present 1.5 cm spacing between the first pair, and these will be the efficiencies reported.

In this report, the efficiencies of cells made earlier, such as those from runs 16-184, 16-187, and all runs from JPL No. 1 up to 18-142 which are presented in Tables VIII and IX, respectively, have been measured using the setup with the probes shorted. The results on 18-143, 148 and 150 in Table X, which have been measured more recently, were obtained with a separate voltage probe, 1.5 cm distant from the nearest current probes.

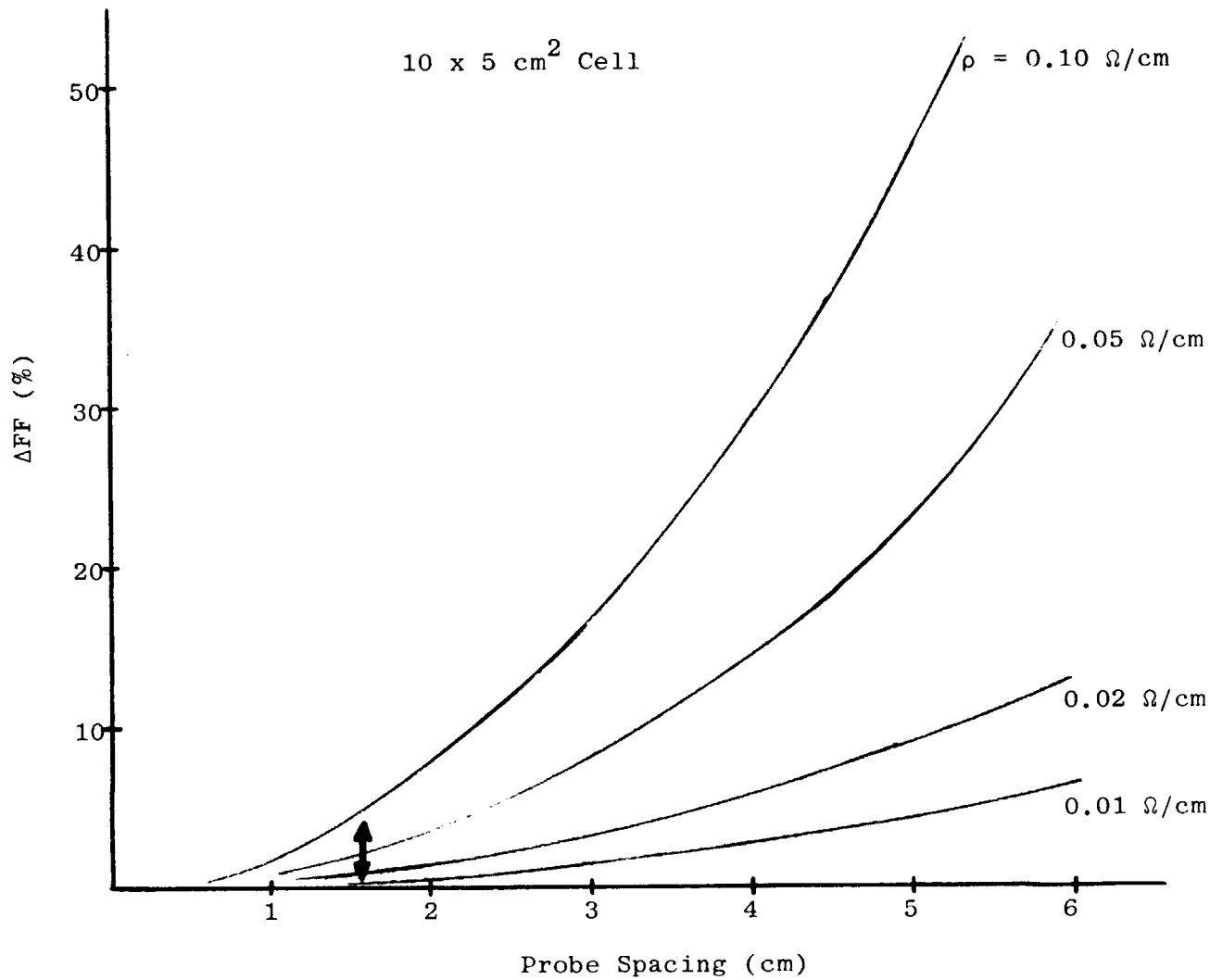

Fig. 6. "Worst case" calculation for the percentage change of fill factor, ΔFF, as a function of the probe spacing and bus bar resistance in a typical 10 cm x 5 cm ribbon cell. See text for more details. The arrowed region is appropriate in our measurements.

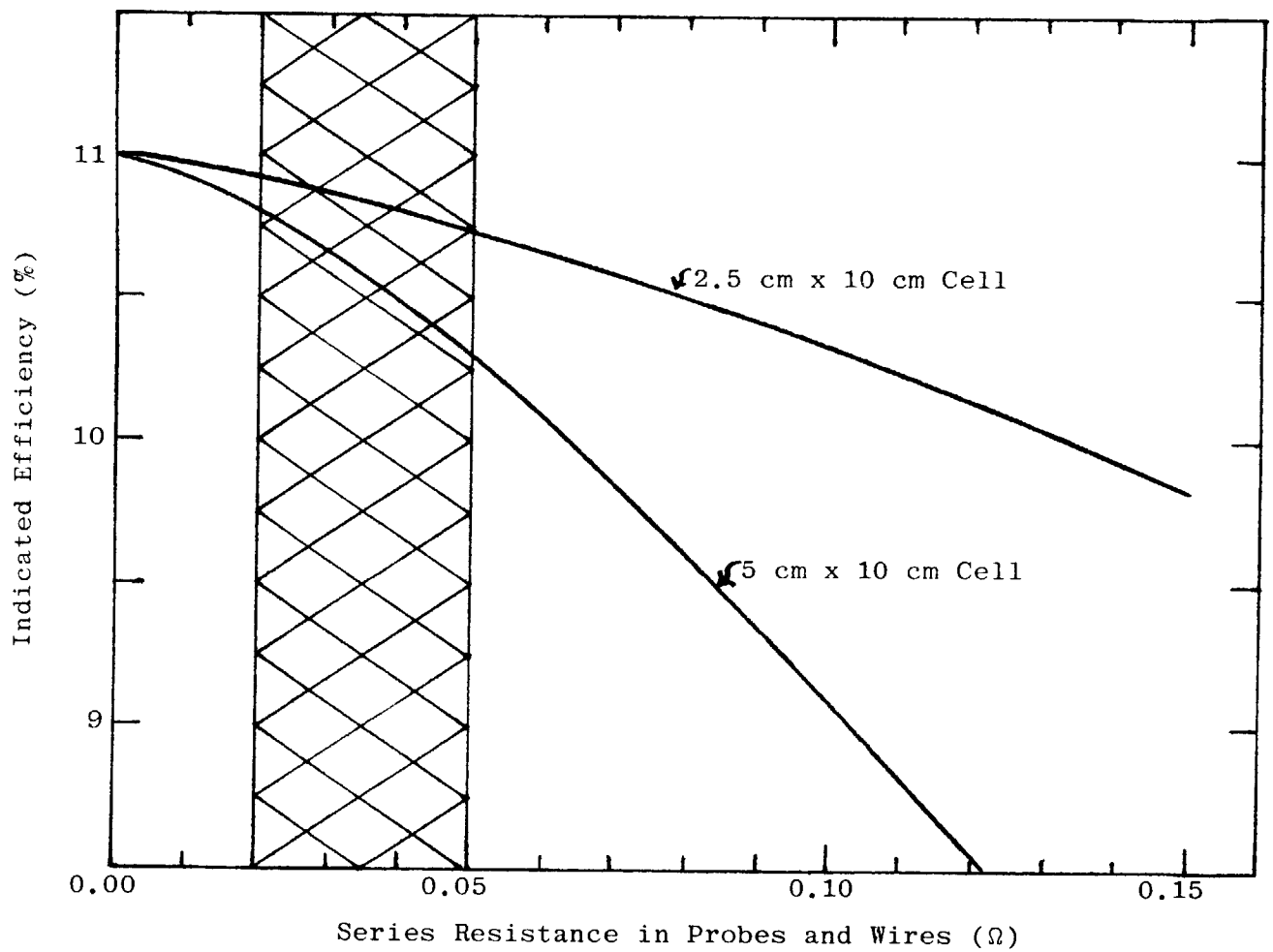

Fig. 7. Calculated efficiency loss due to the series resistance in the measurement setup.

B. Materials Characterization by J.F. Long and M.C. Cretella

1. Electrical Measurements

Among the series of growth parameter experiments performed this quarter in Furnace No. 1, increases in material quality, as reflected by average minority carrier diffusion lengths, appear to have been realized within a matrix of main zone gas purge experiments. Table XI presents all growth run averages.

Although no gains were realized in Furnace No. 3, the previous highest single ribbon growth run average diffusion length (~24 μm) was closely approached over the entirety of the latest multiple growth run for all five cartridges. All diffusion lengths have been reduced via the new data reduction program.

2. Furnace No. 1

a. Cold Shoe Experiment

Two runs early this quarter completed the third series of clean runs initiated last quarter. Run 18-137 was grown without a cold shoe, while run 18-138 utilized a molybdenum cold shoe. The diffusion length averages (18.4 and 18.6 μm, respectively) reinforce the conclusion that such changes have no first order effects on material quality at this level of performance.

b. Baseline Run

A single baseline run was undertaken this quarter under standard experimental system conditions. Run 18-142 had an average diffusion length at 21.7 μm, which had been typical of Furnace No. 1 material performance up to that point.

c. Die Top Modification Experiments

Runs 18-141, 144, and 146 all utilized dies which were modifications of the standard displaced die. The dies used for runs 141 and 144 both had nonuniform top slot widths and were radiused 127 and 63.5 cm, respectively. The die used for run 146 was uniform in top slot width, and was radiused 63.5 cm. The diffusion length averages (22.3 μm, 20.6 μm, and 25.5 μm) do not indicate any advantage to either of the two parameter modifications in terms of material quality enhancement. Additional runs of this nature are planned.

Table XI. Minority Carrier Diffusion Length Averages for Runs done in JPL No. 1.

Run No.	L_D (μm)	Main Zone Argon Purge Rate
18-137	18.4	10 ℓ/min
18-138	18.6	10 ℓ/min
18-140*	26.5	Variable
18-141	22.3	10 ℓ/min
18-142	21.7	10 ℓ/min
18-143*	24.4	Variable
18-144	20.6	10 ℓ/min
18-145*	15.7	Variable
18-146	25.5	10 ℓ/min
18-147**	34.4	~0
18-148*	25.5	Variable
18-149*	29.4	Variable
18-150**	36.5	~0
18-151	35.2	2 ℓ/min
18-152†	25.4	2 ℓ/min

*These runs were done under conditions of varying argon purge rates and surface film in which steady-state conditions were not generally achieved. See discussion in text and Table XII.

**These runs were characterized by a continued buildup of film during the course of the run.

†This run utilized a die without a displacement.

d. Main Zone Purge Gas Experiments

Nine runs of a purge gas experimental matrix were characterized this quarter. These runs were 18-140, 143, 145, 147, 148, 149, 150, 151, and 152. Decreases in the main zone purge have been observed to cause the buildup of a surface film. However, this film completely etches away in the first ten or so seconds of the standard 90 second 4:0:1 etch that is performed prior to Schottky barrier fabrication. Diffusion length averages in the 30 to 40 μm range were observed for three runs at low or zero flow rates (18-147, 150 and 151). Further, within run 18-148, in which the flow rate was gradually reduced to zero with an accompanying buildup of film, the sample diffusion length averages were seen to steadily increase (Table XII(a)). The diffusion lengths in run 18-150 represent a new high level for as-grown material from Furnace No. 1 (Table XII(b)).

3. Furnace No. 3A

The series of runs characterized this quarter included 16-181, 184, 185, 186, and 187. Run 16-181 was a developmental run in which clean procedures were not observed. The material was found to possess high SiC densities on both "A" and "B" surfaces. Minority carrier diffusion lengths were low as well ($\overline{L}_D$ = 7.1 μm).

Run 16-184 was a single cartridge run which employed melt replenishment over an 18 hour period. Four-point probe resistivity measurements indicated an average of 1.1 Ω-cm, with only minor deviation as a function of run time, which indicates that the current scheme of periodic insertion of dopant pellets in the charge rods is successful. Diffusion lengths appeared to rise slightly as a function of run time (Fig. 8), and the average for the run (19.2 μm) is comparable to prior achievements with the old, short hot zone.

Run 16-185 was a multiple ribbon growth run. Material from each of the five cartridges was examined, with samples selected every hour for seven hours of run time. Four-point probe measurements showed anomalously low resistivity values for each cartridge (about .4 to .7 Ω-cm) which rose steadily to about 1 Ω-cm as a function of time (Fig. 9). The solid charge used at the beginning of the run was augmented with silicon chips, the chemical purity of which has recently been questioned. Presuming no error in the initial doping, it is possible that these chips served as a source of contamination which was later diluted by replenishment. Minority carrier diffusion lengths also indicate an upward trend

Table XII. Examples of Diffusion Length Variations During Runs with Main Zone Argon Purge Rate Experimentation.

a. Variable Purge Rate Experiment

Ribbon No.	Purge Rate (ℓ/min)	Film Condition	L_D (μm)
18-148-2	8	None	17.5
-3	8	None	19.5
-4	4	None	26.1
-5	2	Very Light	24.4
-6	0	Light	27.5
-7	0	Moderate	35.2
-8	8	None	29.0

b. Zero Purge Rate

Ribbon No.	Time from Start of Growth (hours)	Film Condition	L_D (μm)
18-150-1	0 - 1	Light	35.1
-2	1 - 2	Moderate	52.3
-3	2.5 - 3.5	Moderate	39.7
-4	3.5 - 4.5	Moderate	33.2
-5	4.5 - 5	Heavy	29.4
-6	5 - 5.5	Heavy	29.1

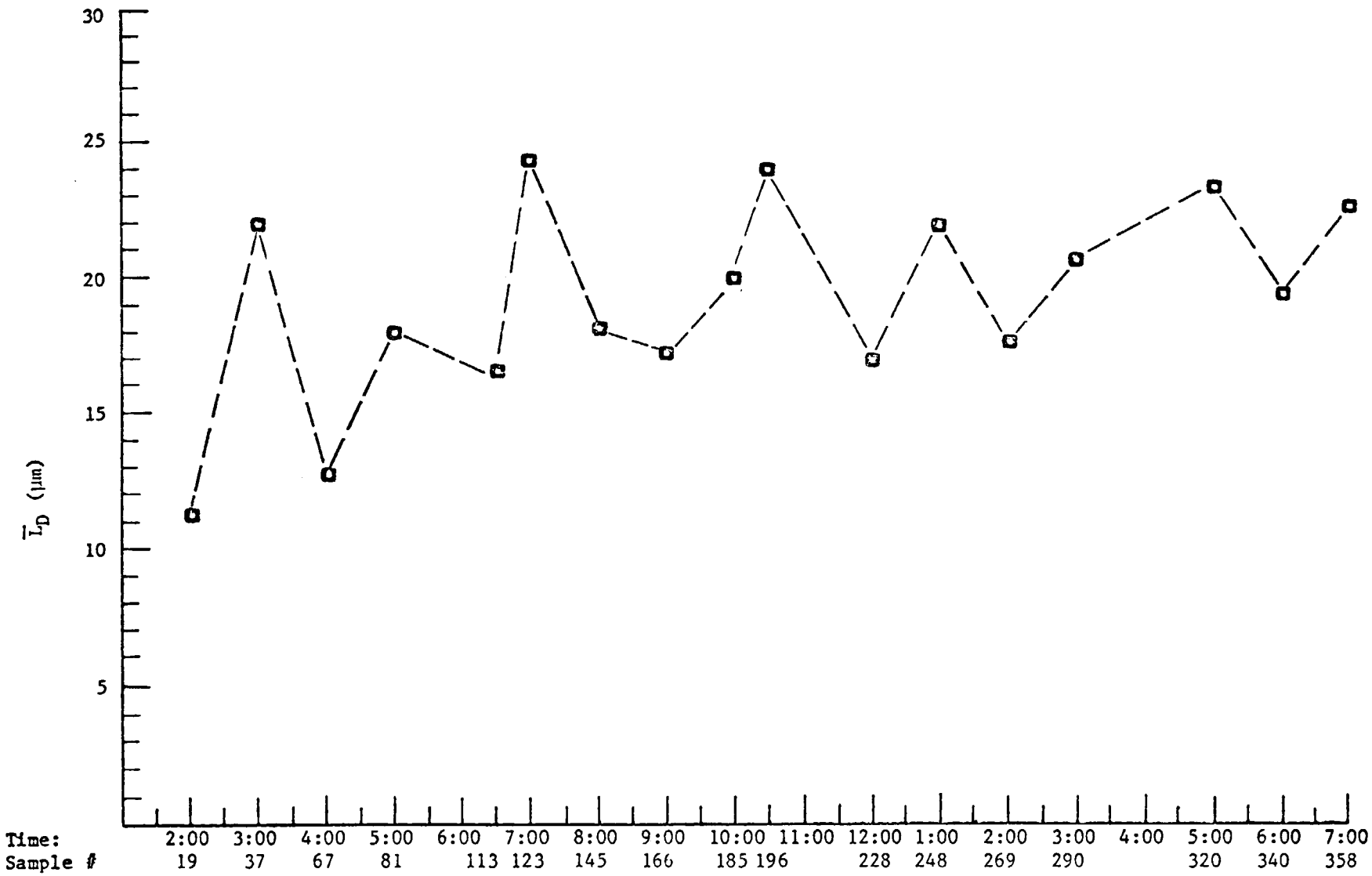

Fig. 8. Minority carrier diffusion length (sample average) vs. time for run 16-184.

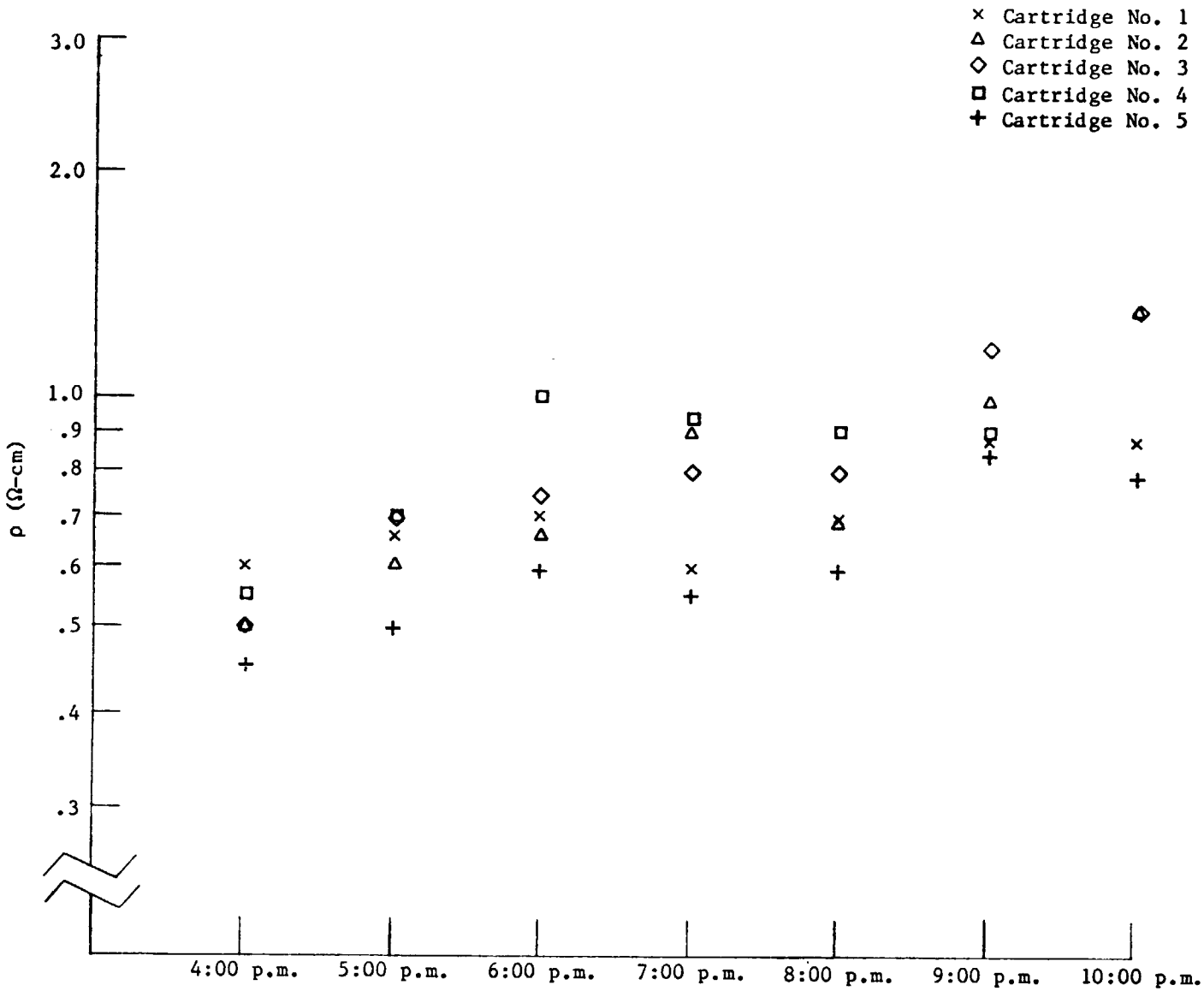

Fig. 9. Four-point resistivity vs. time, five-ribbon run 16-185 (second half of run only).

with time (Fig. 10), which lends support to this possibility. "A" (high meniscus side) surface SiC particle densities were found to drop very sharply as a function of time as well (Fig. 11).

Run 16-186 was a single-cartridge run which employed a previously used crucible. It was thought that the incidence of SiC particle inclusion could be lowered if carbon could be prevented from dissolving into the melt; hence a crucible was used which had been SiC-coated via previous use (see Section III).

The highest "A" surface SiC particle density observed for six samples examined was $.16/cm^2$. Further, all but one of the particles were located within 2 mm of the sample edge. The average minority carrier diffusion length (17.7 μm) was not depressed, in spite of the employment of a used crucible which had not been handled in a strictly clean fashion.

Run 16-187 was undoubtedly the most successful multiple run to date. Samples from all five cartridges (a total of 47) were examined for diffusion length. Cartridge averages were fairly tightly distributed (19.7 μm to 24.4 μm); the run overall average (21.3 μm) was very close to the optimum observed for this system in single-cartridge mode (about 24 μm), and no degradation with time was observed for any of the cartridges (Fig. 12).

C. Microscopic Crystallographic and Chemical Studies on Ribbons from the "Gas Flow" Experiments

As mentioned above, as the argon gas flow inside the growth station (Furnace No. 1) is reduced, a film begins to appear as the first visible sign of a change in growth conditions. At the same time, on both sides of the ribbon, the surface becomes completely clear of discrete SiC particles. This film, which becomes thicker with decreasing gas flow, has been identified using IR spectroscopy as a mixture of primarily SiC with some SiO_x. The IR spectra were taken of both a low and a high gas flow sample before and after etching. The absorption peaks observed before etching for the low gas flow included one at 790 cm^{-1}, associated with Si-C bonds, and a small peak at 1100 cm^{-1}, associated with Si-O bonding. After etching, the peak at 790 cm^{-1} is absent and the absorption at the 1100 cm^{-1} peak is slightly diminished. For the high gas flow sample before etching, no peak was observed at 790 cm^{-1} and a small peak was observed at 1100 cm^{-1}. After etching, no change is observed in the peak at 1100 cm^{-1}. Additionally, photomicrographs of the filmed sample show a uniform coverage of the surface which appears to include two distinct features. One feature indicated in the photomicrograph of Fig. 13(a) is dispersed in the other which is a dendritic-like matrix. Soaking of the sample in 20%

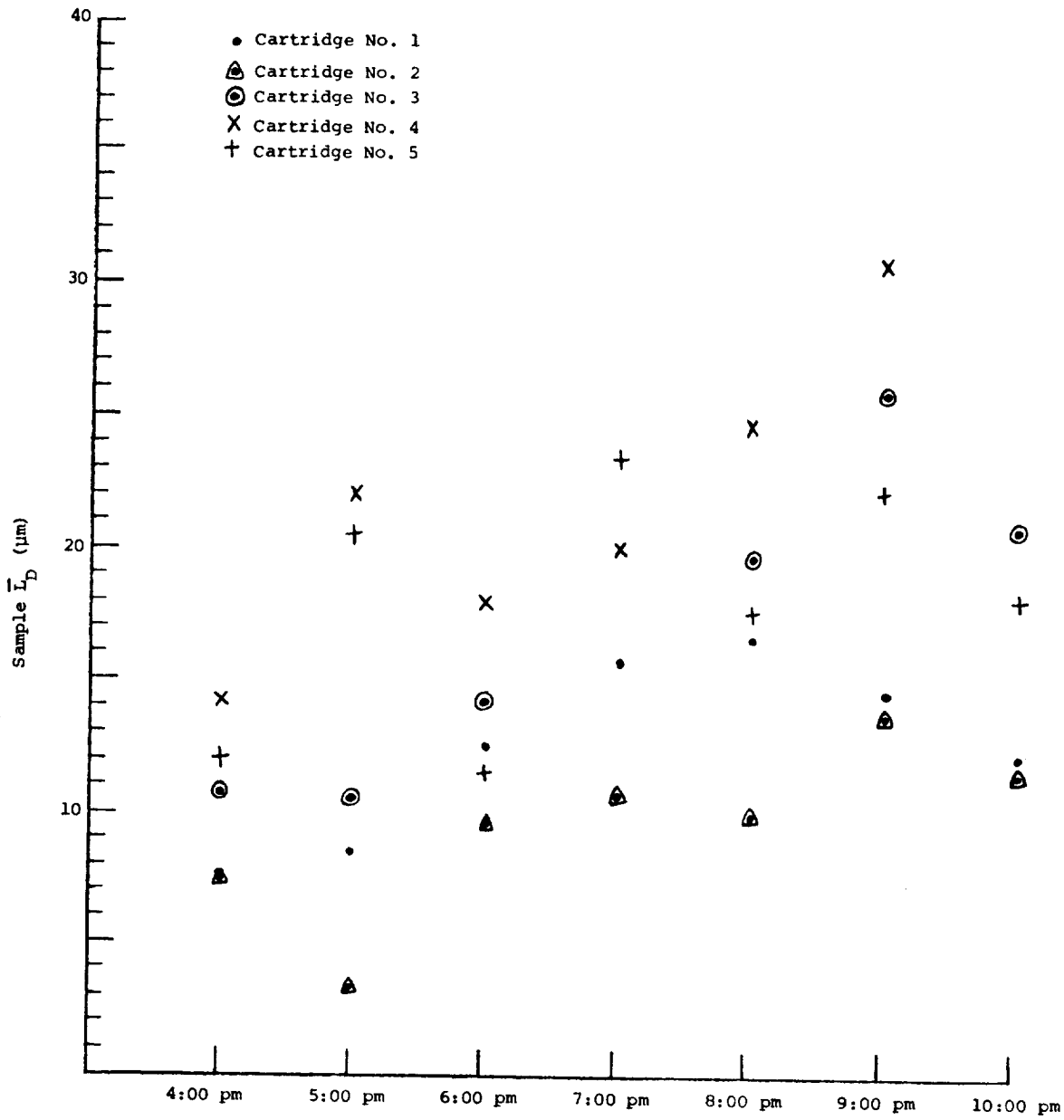

Fig. 10. L_D vs. time, five-ribbon run 16-185 (second half of run only).

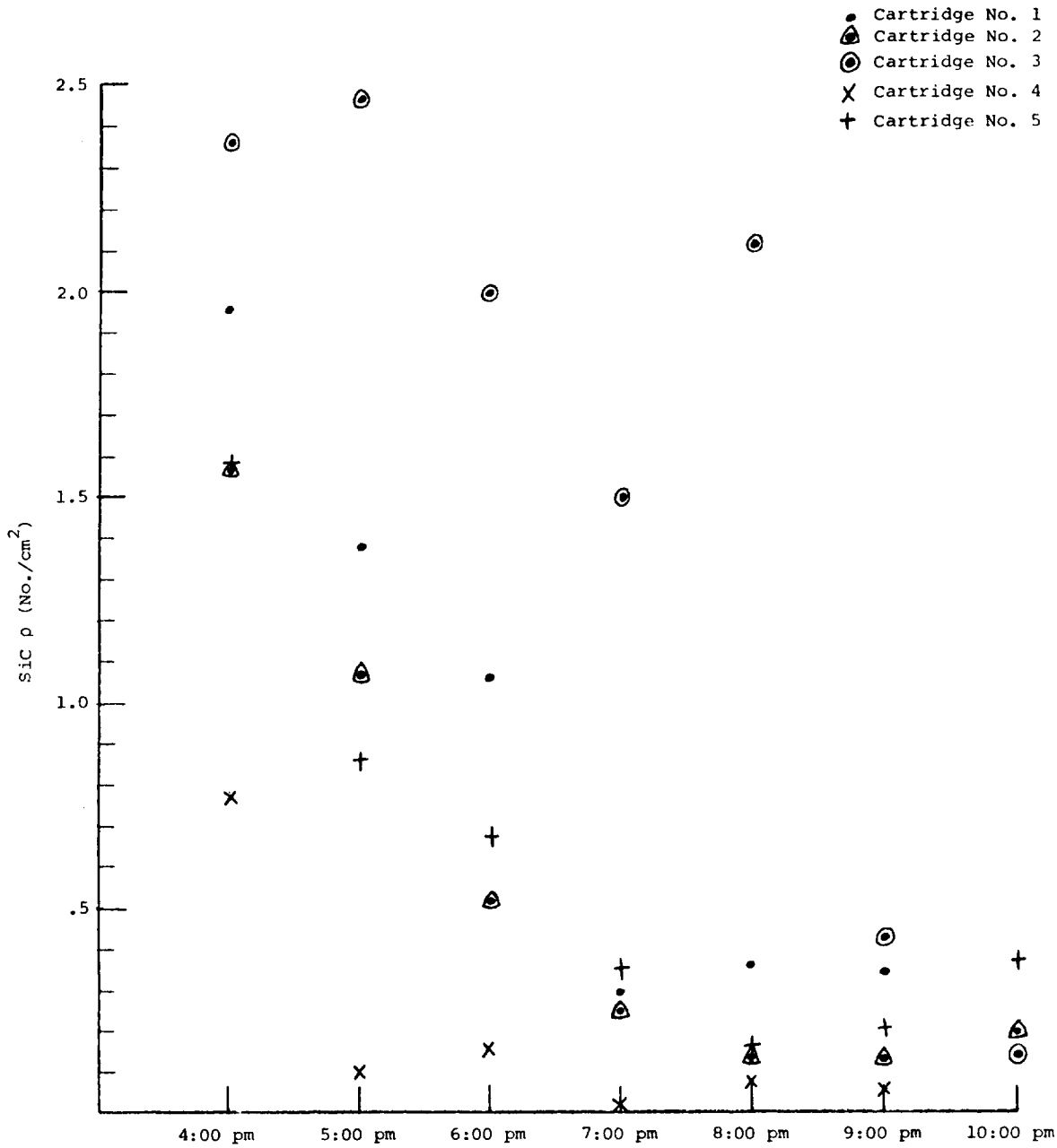

Fig. 11. Silicon carbide particle surface density vs. time, five-cartridge run 16-185 (second half of run only).

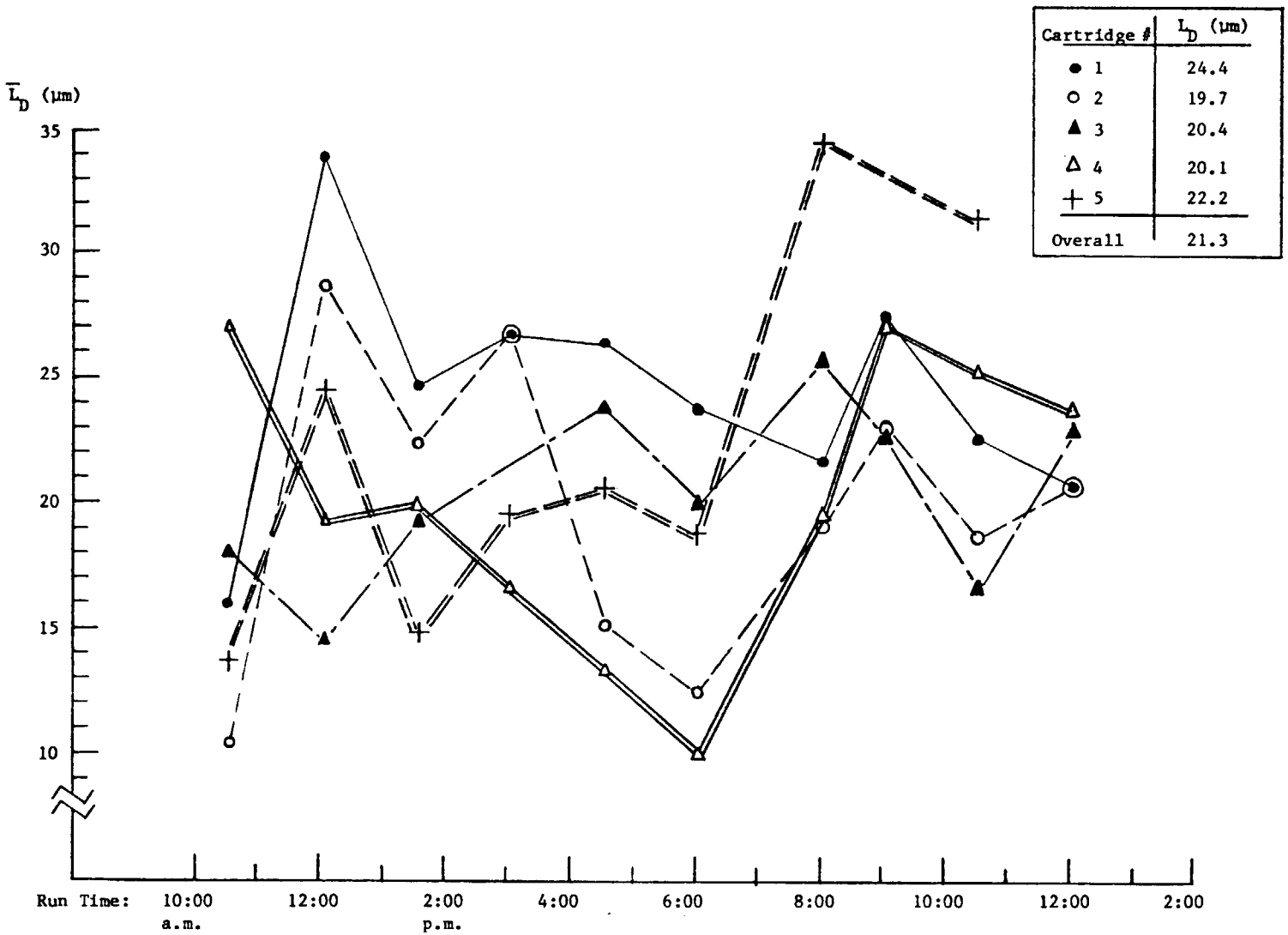

Fig. 12. Sample average diffusion lengths for multiple growth run 16-187.

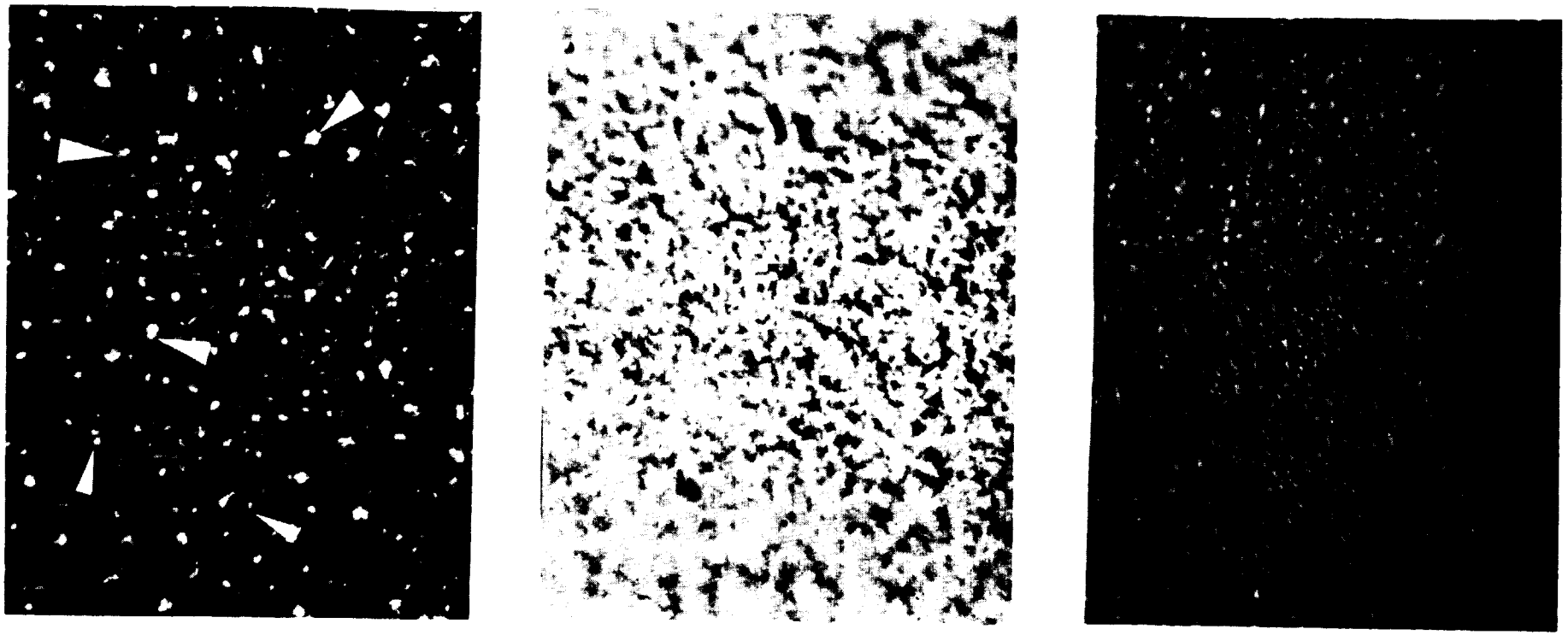

(a) (b) (c)

Fig. 13. Photomicrographs of heavy film which appears on silicon ribbon grown with very much reduced gas flow. (a) "As-grown" film. Particle-like feature (as indicated by arrows) appears as a dispersion in second feature of film. (b) After 48 hours' etching in 20% HF, particles shown in (a) have dissolved leaving this insoluble SiC dendritic matrix. (c) Uniform micropitting observed on the silicon surface where the film had sloughed off during HF dissolution. Mag. 1800X.

HF (a solvent for SiO_x) for 48 hours left only the dendritic film structure shown in Fig. 13(b). Sections of the film, which detached from the surface during dissolution, gave the X-ray diffraction pattern of SiC. The surface of the silicon where the film had sloughed off was uniformly micropitted as shown in Fig. 13(c). Hence, one general conclusion might be that the reduction in gas flow somehow affects the nucleation of SiC, i.e., its nucleation frequency is now increased to such an extent that a SiC film is formed instead of the much larger SiC particles which are usually seen on the ribbon. An investigation of the response of the cross-sectional structure to the reduced gas flow reveals an apparent development (whether in distinct stages or continuous, we cannot yet say) from the typical, somewhat disrupted, structure of the normal ribbon grown from this station (JPL No. 1) (Fig. 14(a)) to the much cleaner structure (Fig. 14(b)) which has been usually associated with 2.5 cm wide ribbon grown in RF heated machines. This, then, is the cross-sectional manifestation of the structure that has become known as the "equilibrium defect structure" of EFG ribbon.[4]

However, in the extremes of the growth conditions, which always imply the presence of a heavy surface film so far, we obtained structures distinctly different (Fig. 14(c)). This becomes even more apparent when we examine the surface structure of etched ribbon segments (Fig. 15). Here we have developed very large (5 mm wide, 10 to 20 cm long) grains (Fig. 15(b)), which may or may not be bounded by twins and may or may not be aligned with the growth axis. This, obviously, is no longer an "equilibrium defect structures" (Fig. 15(a)).

Hence, these experiments demonstrate for the first time that there exist conditions under which a ribbon containing the "equilibrium defect structure" can be converted into a very large grained polycrystalline silicon sheet during EFG growth. Thus, these experiments open up the possibility of producing single crystalline EFG ribbon from carbon crucibles and dies in the future.

(a)

(b)

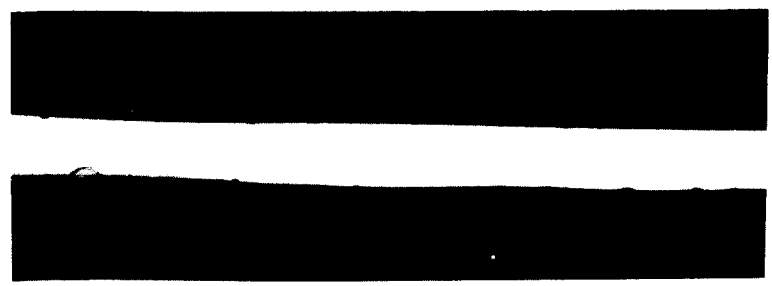

(c)

Fig. 14. Cross sections of silicon ribbon which have been syton-polished and etched in the Sirtl etchant. (a) Cross-sectional structure shown is typical of normal ribbon grown with standard gas flow. (b) Cross-sectional structure shown is typical of equilibrium defect structure and was obtained from samples of ribbon grown at reduced gas flow. (c) Cross section of large grain obtained in ribbon grown at much reduced gas flow; heavy film growth had occurred. Mag. 45X.

(a)

(b)

Fig. 15. Surface structure of ribbon segments etched in 30% KOH solution to remove surface film and reveal grain structure. (a) Typical equilibrium defect structure, grown with reduced gas flow and associated moderate surface film. (b) Large single crystal grain growth developed at very much reduced gas flows with heavy surface film growth. Mag. ~.9X.

V. MACHINE 17 by E. Sachs and A. Menna

A. Overview

In this section, we will summarize the first series of experimental runs relating to stress studies and the conclusions based on them. Also, a detailed study of the dynamic response of an EFG system to various possible control inputs has been completed now. This work is summarized in the form of a preprint as Appendix 7 to this report and is, therefore, not further discussed in this section.

B. Experimental Studies and Conclusions on Stress in Ribbon

The experimental program is comprised of 17 runs to date done over the course of three months. The first ten of these were performed on a system with no cold shoe, while a mini cold shoe was used on the last seven of these runs.

1. Runs Without the Cold Shoe

As described previously, it has been suggested that the elastic strain field caused by a curvature of the vertical temperature profile could be counteracted by appropriate shaping of the horizontal isotherms. The primary goal of the experiments conducted on the system without the cold shoe was to investigate this hypothesis.

It was intended to quantify first the stress levels resulting from a system with basically horizontal isotherms for a series of afterheater temperatures. Thus, the first seven of the ten runs in this series were done on identical systems, all with uniformly heated afterheaters. The only difference from run-to-run was the afterheater thermocouple setting, which ranged from 1015°C to 1170°C. This series of runs was also used to evaluate the stress measurement technique described earlier.

It was found that correlation did exist between afterheater setting and ribbon stress level. Any setting below 1015°C made it impossible to

grow whole ribbon -- it would invariably split in the belt puller. As the temperature was increased, the stress levels decreased in a repeatable fashion, the ribbon grown at 1170°C having no apparent stress. The relative measurement of stress is based on two factors: (i) breakage and handling, and (ii) central scribe and split technique.

As noted above, detailed stress measurements are being made all through this series of runs, especially by the multiple cut and split technique. Unfortunately, as noted in the previous section, these measurements are of questionable validity and, in general, did not seem to indicate the large differences in stress being observed by the more elementary approaches.

In the last three of the no-cold shoe experiments, the heating element in the afterheater was reshaped to yield heating preferential to the center (experiments 8 and 9) and preferential to the edges (experiment 10) in order to evaluate the effect of horizontal isotherm shape. In the first case, the reshaped heater yielded twice the power dissipation in the central 3.2 cm of the 7.6 cm afterheater, while in the second case the power dissipation was twice as great for the outer 2.5 cm length as compared with the center length.

The experiments with the preferentially center-heated afterheater seemed to indicate slightly lower stress levels for the same afterheater thermocouple setting than in the case of a uniformly heated afterheater. In fact, the second of these was done with the afterheater at 970°C. While this ribbon was highly stressed, it did at least emerge unbroken. The experiment with the preferentially edge-heated afterheater was carried out at an afterheater setting of 1015°C. The stress level observed was perhaps slightly higher than that seen for a uniformly heated afterheater.

The theory would indicate that the center-heated afterheater (concave down horizontal isotherms) should ameliorate the stress, while the edge-heated afterheater should exacerbate it. While the results did seem to indicate agreement, the differences noted in stress level were just too small to be meaningful. It should be noted, however, that the preferential heating did indeed have an effect all the way down to the interface, as the interface shape was considerably affected. In fact, growth with the center-heated afterheater was considerably easier than with the edge-heated device.

2. Runs with the Cold Shoe

As little effect on stress levels was observed with rather

large changes in horizontal profile, it was felt that perhaps it was necessary to grow in a higher speed range (with a cold shoe) in order to see more profound effects.

In the first of the seven growth runs made with the mini cold shoe, the two halves of the shoe were configured to introduce gas differently to the ribbon surface. One half distributed the gas uniformly across the ribbon width, while the other half was blocked off in the center, and introduced gas only at the ribbon edges. Switching the same volume flow rate of gas from the front shoe to the rear allowed for a rapid change in horizontal cooling profile. Growth was carried out at approximately 3.5 cm/min, and the gas was switched from one side to the other, compensating for the changed interface shape with the end heaters. No difference was noted in the stress level or non-flatness of the resultant ribbon. However, the stress level was low, and perhaps did not allow for much improvement.

The second of the seven experiments was designed to assess the importance of residence time in a given thermal profile. After ~1 meter of growth, grown at ~3.5 cm/min, the growth speed was lowered to ~2 cm/min, thus allowing for more residence time. The uniformly heated afterheater was kept at 1070°C, and the cold shoe gas flow was uniformly distributed. Little difference was noted in stress level. Possibly again there was insufficient room for improvement.

The last five runs were all attempts to simply grow fast, wide flat ribbon. The speed was successively increased by using a bulbous die for the last three runs and thinning the die top down. The result was that in the last run, 7 cm wide, .02 to .03 cm thick ribbon was grown at 5.0 cm/min. It was found to be minimally stressed and fairly flat. The deviations from flatness were long in wavelength (not abrupt buckles), and corresponded largely to the area between the guide ribs in the afterheater plates. Finally, it should be noted that several of these runs produced ribbon which, when split, demonstrated a tendency to overlap, the opposite of the more common tendency. This might prove to be a good point of departure for future stress studies.

REFERENCES

1. F.V. Wald et al., "Large Area Silicon Sheet by EFG," Second Quarterly Progress Report, DOE/JPL 954355/78-2 (July 1978).

2. B.H. Mackintosh et al., "Large Area Silicon Sheet by EFG," First Quarterly Report, ERDA/JPL 954355/77-1 (March 1977).

3. H.B. Serreze, in: 13th IEEE Photovoltaic Specialists Conference Record (New York: IEEE, 1978), p. 609.

4. L.C. Garone et al., Appl. Phys. Lett. 29 (1976) 511.

PAGE 62 INTENTIONALLY BLANK

APPENDICES

1. Updated Program Plan

The program plan shown previously is still in effect.

2. Man Hours and Costs

Previous cumulative man hours were 67,640 and cost plus fixed fee was $2,367,186 through the first quarter of 1979. Man hours for the second quarter of 1979 are 5,404 and cost plus fixed fee is $210,435. Therefore, total cumulative man hours and cost plus fixed fee through June 1979 are 73,044 and $2,577,621, respectively.

3. Engineering Drawings and Sketches Generated During the Reporting Period

None.

4. Summary of Characterization Data Generated During the Reporting Period

These data are contained in Section IV. Note that large area (~50 cm^2) cells are reported which have efficiencies over 11% (AM1). Also note in particular the discussion on methods of cell efficiency measurement appropriate for large cells and the change in method made.

5. Action Items Required by JPL

None.

6. New Technology

New technology is being separately reported, pending possible patent applications.

7. Other

Preprint: "EFG Dynamics as Related to Automatic Controls Development," by E. Sachs.

PAGE 64 INTENTIONALLY BLANK

APPENDIX 7

Preprint: "EFG Dynamics as Related to Automatic Controls Development"

by E. Sachs

PAGE 66 INTENTIONALLY BLANK

INTRODUCTION

In the growth of ribbon by the EFG process, the geometry of the grown crystal is determined by the meniscus height across the width of the ribbon and the position of the ribbon edges. It is therefore necessary to control these geometric parameters during growth in order to produce ribbon of uniform thickness and width.

Fundamentally, this control is exercised by modifying the temperature field of the die and other growth parameters, notably the pulling speed. In one method, the temperature field of the die is modified by three independent resistance heaters, one along the length of the die and one at each die edge. In such an arrangement, the meniscus height along the width is largely determined by the power dissipated by the full length die heater and the pulling speed. The position of the edges is determined by a more complicated interaction of speed, die shaping, meniscus height at the edge, and edge die heater power levels. This paper will be primarily concerned with the meniscus height along the ribbon width.

Traditionally, meniscus height is controlled by selecting a pulling speed and varying the die heater power level to establish the proper meniscus height. The die heater power level is not controlled directly by the meniscus height, but rather by a thermocouple near the die which provides an analogue measurement of the die temperature. Raising the temperature set point of this thermocouple increases the average die heater power level and raises the meniscus. However, it is the operator who must determine by visual observation whether the meniscus height is acceptable, too high or too low, and make appropriate changes to the temperature set point of the die heater controller. Thus, while the die heater is operating in a closed loop mode based on a temperature measurement, it is the operator who must finally close the control loop by visual observation.

A more direct control system would control die heater power and pulling speed by direct measurement of the meniscus height. Such a control system would obviate the need for operator intervention and improve the immunity of the system to transients, and other external factors. It is the consideration of such a control system which prompts this investigation.

However, the proper design of any control system, whether it is temperature or meniscus height based, is predicated on an understanding of the system being controlled. A thorough understanding and modeling of the dynamics of the system will make possible the design of an optimal control system as well as point out how the system might be modified to improve its performance.

ELEMENTS OF THE CONTROL SYSTEM

Figure 1 presents two schematic block diagrams of a meniscus height control system based on direct measurement of meniscus height; Fig. 1(a) relying on pulling speed actuation, while Fig. 1(b) relies on die heater modulation. In both cases the measured meniscus height is subtracted from an operator selected meniscus height set point. The error signal thus generated is fed into the control electronics, and a control signal is produced.

In Fig. 1(a) this control voltage is then used to control pulling speed by means of a tachometer controller servomotor. This servomotor actually comprises a separate control loop lying wholly within the one now under consideration. Its precise nature need not concern us here as we assume that it responsed much more quickly than the system we are trying to control. The pulling speed then acts on the EFG system to yield a meniscus height for a given (and constant) die heater power level.

In Fig. 1(b), the control voltage is fed to a power amplifier, the output of which goes directly to the die heater. The power dissipated on the die heater then acts on the composite system yielding a meniscus height for a given (and constant) pulling speed. This composite system is indicated as being composed of a heater-die thermal system and a separate EFG system.

In order to design the control electronics in these systems, we must understand the dynamics of all other elements in the control loop. We will start by examining the physics of the EFG process, in particular the relations between meniscus height and pulling speed and between meniscus height and die temperature. Later, we will model the die-heater system as a lumped parameter thermal system.

Three independent experiments will serve to gauge the validity of these models:

1. The effect of changes in pulling speed on meniscus height and ribbon thickness will be observed while keeping the die heater power constant. This will serve to test the models of EFG physics per se.

2. The effect of changes in die heater power on die temperature will be observed. This will test the lumped parameter thermal models.

3. The effect of changes in die heater power level on meniscus height and ribbon thickness will be observed for constant pulling speed. This experiment is a synthesis of the above two as it incorporates both the dynamics of the thermal system and the dynamics of the EFG process itself. This will allow us to test the validity of treating the thermal system and the EFG system as separate entities.

Finally, it should be noted that these models and experiments will allow us to design either a velocity or die heater actuated control system, or any combination of the two. It may in fact prove necessary to effect control of the meniscus by both pulling speed and die heater modulation.

REVIEW OF PHYSICS OF EFG PROCESS

We may divide our analysis of EFG into two components: the steady-state, and the dynamic response. The steady-state analysis will allow us to relate meniscus height, ribbon thickness, growth speed, die temperature, and other system parameters for steady-state growth. This information will also yield the steady-state sensitivities of the growth. For example, if a small change

is made in pulling velocity around some steady-state operating point, we will be able to predict the resulting ribbon thickness after a new steady-state is reached. However, for information on how the growth responds to transients, e.g., how it proceeds from one steady-state to another, we must turn to the complete dynamic analysis.

An essential element of both analyses is the relationship between the geometric variables involved in the meniscus controlled shaping action that is EFG. As indicated in Fig. 2, along the face of the ribbon the meniscus may be assumed to be a circular arc, the radius of which is determined by Laplace's equation. The other relevant geometric parameters are the die dimension t_d, the meniscus height s, the ribbon thickness t, and the meniscus angle ϕ defined as the angle between the meniscus and the vertical at the interface. For growth of constant thickness ribbon it has been found [1] that ϕ must attain a specific non-zero value called ϕ_o. For silicon, $\phi_o \cong 11^o$. These parameters may be related as follows:

$$t_d - t = 2[R \cos \phi - (R^2 \cos^2 \phi - s^2 - 2sR \sin \phi)^{\frac{1}{2}}]. \qquad (1)$$

The steady-state relationship among the growth variables is determined by energy conservation at the growth interface. If Q_{ribbon} represents the heat conducted up the ribbon from the interface, Q_{fusion} the heat of fusion generated at the interface, and Q_{men} the heat conducted to the interface through the meniscus, all per unit width and time:

$$Q_{men} + Q_{fusion} = Q_{ribbon}. \qquad (2)$$

At this stage, heat transfer and geometric models must be chosen, and the three heat fluxes in Eq. (2) must be restated in terms specific to these models. At that point, steady-state sensitivities of the growth may be determined from the energy conservation conditions [2], as discussed earlier. As an example, we give one such steady-state sensitivity taken in the limit as the growth speed approaches V_{max}, the maximum growth speed of the

system for thickness t:

$$\left.\frac{\partial t}{\partial V}\right|_{ss} = \frac{-t}{2V_{max}}, \tag{3}$$

where the subscript ss denotes steady-state.

In order to describe the complete dynamic behavior of an EFG system, one must write the following set of equations describing the time evolution of the crystal shape [3]:

$$\dot{t} = 2V_g \tan(\phi - \phi_o) \tag{4}$$

$$\dot{s} = V_p - V_g \tag{5}$$

$$V_g = V_g(t, s, T_d) \tag{6}$$

$$\phi = \phi(t, s), \tag{7}$$

where V_g is the growth speed, V_p is the pulling speed, T_d is a die temperature, and differentiation with respect to time is denoted by a dot.

Equations (4) and (5) embody the dynamics of the EFG process. Equation (4) is a consequence of the meniscus angle requirements for steady-state growth. Equation (5) is a statement of geometric compatibility. Equations (6) and (7) are restatements in functional form of the geometric and energy conservation conditions discussed earlier.

Equations (4) through (7) are the basic equations needed to describe the dynamics of an EFG growth process, and, more generally, any meniscus-controlled growth process. However, they are a complex set of nonlinear equations, and hence are not amenable to analytical treatment. A linearized analysis of this set of equations can, however, serve as a starting point in the dynamic analysis.

Thus, we will examine the dynamic behavior of the system about an operating point by linearizing the equations about that point. We will denote the steady-state values of the parameters by the subscripts "o". Partial derivatives at steady-state will be denoted by the subscript ss. The result of such a linearized analysis [3] are the following two differential equations for

ribbon thickness and meniscus height:

$$\ddot{t} + 2\xi\omega_n\dot{t} + \omega_n^2 t = \left.\frac{\partial t}{\partial V}\right|_{ss} \omega_n^2 \left[V_p - \frac{\partial V_g}{\partial T_d} T_d\right] \tag{8}$$

$$\ddot{s} + 2\xi\omega_n\dot{s} + \omega_n^2 s = \dot{V}_p + \omega_n^2 \left.\frac{\partial s}{\partial V}\right|_{ss} V_p - \frac{\partial V_g}{\partial T_d}\left[\omega_n^2 \left.\frac{\partial s}{\partial V}\right|_{ss} T_d + \dot{T}_d\right] \tag{9}$$

where

$$\omega_n^2 = 2V_{go} \left.\frac{\partial \phi}{\partial s}\frac{\partial V}{\partial t}\right|_{ss} \tag{10}$$

$$2\xi\omega_n = \left(\frac{\partial V_g}{\partial s} - 2V_{go}\frac{\partial \phi}{\partial t}\right). \tag{11}$$

These equations are second-order linear ordinary differential equations. As should be expected, the characteristic equation (the terms on the left sides) have the same form for the two system parameters t and s, since they are variables in the same system. Such a second-order system is characterized by two parameters, the natural frequency ω_n and the damping ratio ξ. When the damping ratio is zero, an undamped system will respond to an initial step disturbance by oscillating at the natural frequency. A system with damping ratio between 0 and 1 will respond to an initial step disturbance with decaying oscillations with a frequency slightly smaller than ω_n. Finally, an overdamped system with $\xi > 1$ will respond to an initial step disturbance with a nonoscillatory, exponential approach.

The forcing function, or right hand side is, however, different for Eqs. (8) and (9). In other words, external inputs will have different effects on the two system variables t and s. Note that the forcing function for both equations involves V_p and T_d. Thus, if we were interested in the response of the meniscus height to changes in pulling speed, we would examine Eq. (9) with $T_d \equiv 0$. Finally, it should be pointed out that the steady-state response to constant inputs (obtained by equating all time derivatives to zero) does not follow directly from the dynamic theory, but must be determined from the energy conservation statement (Eq. (2)) as discussed previously.

EXPERIMENTAL PROCEDURE

The dynamics of a system may be most easily tested by frequency response techniques. In such a procedure, a sinusoid is used as the input to a system. The output from the system is then observed after the system has reached its steady state. If a system is linear, then the output must also be a sinusoid of the same frequency as the input. Measurements are then made of the amplitude of the output as well as its phase relationship with the input. From this data, we construct "Bode" plots where we plot the log of the output against the log of the frequency, and the phase shift of the output against the log of the frequency. In a Bode plot, the magnitude of the output is normalized by the magnitude of the input. That is, we divide the peak-to-peak sinusoidal response of the system by the peak-to-peak sinusoidal input thus eliminating the dependence of the response on the input amplitude chosen for the experiment. An important benefit of this technique is that it allows for easy comparison of the measured data with theoretical prediction, both for amplitude and phase angle response.

In order to perform the series of experiments outlined in the section on the elements of the control system, we must be able to measure pulling speed, die heater power level, meniscus height, and die temperature as outputs during growth. Ribbon thickness is, of course, measured after growth.

The basic observational measurement and recording tool used in these experiments is the anamorphic optical video system shown on the growth furnace in Fig. 3. An anamorphic optical system is one which enlarges more in one direction than the other. When applied to an EFG growth system, anamorphic optics permit us to enlarge the image more in the vertical direction than in the horizontal, thereby maintaining good resolution of the meniscus height (typically .02 cm high) across the full ribbon width (7.5 cm maximum width for the growth system picture). The system shown in Fig. 3 enlarges by a factor of 18 more in the vertical than in the horizontal and displays the resultant image directly on a television monitor.

Figure 4 is a photograph taken directly from the television monitor. The top half of the screen is the view of the growth as seen by the anamorphic optical system. The bottom half of the split screened image is the instrumentation panel as seen by a second TV camera. The top row of digital panel meters provides information on power levels of the die heaters, pulling speed and run time, while the meter at the lower right gives the temperature as recorded by a thermocouple in close proximity to the die. The storage oscilloscope provides a means of simultaneously recording both the input to (bottom trace), and the output from the system (top trace). Thus, the digital meters and the view of the growth itself provide information as to the operating point, while the oscilloscope traces record the fluctuations of input and output around the operating point. For slow oscillations the digital meters can provide more exact information as to the magnitude of the variations. Finally, phase shift of the output may be measured on the oscilloscope tracing. However, this measurement is extremely sensitive to slight deviations of the output from a sinusoidal wavelength due to noise.

System inputs are measured in straightforward manners. Pulling speed is measured directly by the tachometer on the belt puller drive motor. Die heater power is measured by multiplying the true RMS values of die heater current and voltage.

The measurement of system outputs is somewhat more involved. Meniscus height is measured by video-analysis of the anamorphic view of the growth. As shown in Fig. 5, a video threshold is set, above which all the image points are turned white, and below which the image points are turned totally dark. This effectively maximizes the image contrast. A box is then superimposed on the TV screen and the average is taken of all the video intensity falling within it. As the meniscus moves up and down within the box, this averaged video intensity serves as an analogue signal proportional to meniscus height. This meniscus height measurement has excellent resolution (better than 5×10^{-4} cm) as it represents a spatial average of the meniscus.

The die temperature was measured by forming a thermocouple between the carbon die and a silicon ribbon melted and refrozen

to it. The side wall and floor of the growth system cartridge form a continuous graphite conduction path up and out of the furnace. Thus, the junction between the silicon ribbon and the die tip forms a thermoelectric couple, the output of which may be related to the temperature of the die tip. Thermocouples formed by bonding carbon string to silicon ribbon have been used to map the temperature field of ribbon growth systems [4], and hence their thermoelectric behavior is known. The advantage of this technique in this application is that it allows us to measure directly the temperature of the die tip with a ribbon attached, a condition closely approximating growth.

RIBBON THICKNESS AND MENISCUS HEIGHT RESPONSE TO CHANGES IN PULLING SPEED

The response of ribbon thickness and meniscus height to pulling speed is given by Eqs. (8) and (9) with $T_d \equiv 0$. As discussed previously, we will be concerned with the amplitude and phase angle of the response to sinusoidal inputs of frequency ω. Any of several techniques (e.g., Laplace transforms) may be used to derive expressions for these responses from Eqs. (8) and (9). Presented below are the expressions for the amplitude response of thickness $\left(\frac{|t|}{|V|}\right)$, the amplitude response of meniscus height $\left(\frac{|s|}{|V|}\right)$, and the phase angle response of meniscus height to speed changes.

$$\frac{|t|}{|V|} = \frac{\left.\frac{\partial t}{\partial V}\right|_{ss}}{\left[\left(1 - \left(\frac{\omega}{\omega_n}\right)^2\right)^2 + \left(2\xi \frac{\omega}{\omega_n}\right)^2\right]^{\frac{1}{2}}} \tag{12}$$

$$\frac{|s|}{|V|} = \frac{\left[\frac{\omega^2}{\omega_n^4} + \left.\frac{\partial s}{\partial V}\right|_{ss}^2\right]^{\frac{1}{2}}}{\left[\left(1 - \left(\frac{\omega}{\omega_n}\right)^2\right)^2 + \left(2\xi \frac{\omega}{\omega_n}\right)^2\right]^{\frac{1}{2}}} \tag{13}$$

$$\text{phase angle} = \tan^{-1}\left(\frac{\omega}{\omega_n^2 \left.\frac{ds}{dV}\right|_{ss}}\right) - \tan^{-1}\left(\frac{2\xi \frac{\omega}{\omega_n}}{1 - \left(\frac{\omega}{\omega_n}\right)^2}\right) \tag{14}$$

Figures 6 and 7 present frequency response data for both thickness and meniscus height response as well as theoretical calculations based on Eqs. (12) through (14). This data results from a single run and was measured and recorded as described previously. The relevant data for this run is presented below:

$$t_d = 0.061 \text{ cm}$$

$$t = 0.041 \text{ cm}$$

$$s = 0.025 \text{ cm}$$

$$R = 0.073 \text{ cm}$$

$$V_{go} = 0.032 \text{ cm/sec}$$

$$V_{max} = 0.036 \text{ cm/sec}$$

In plotting the theoretical results of Eqs. (12) through (14), it is first necessary to derive the necessary partial and total derivatives from the geometric relation (Eq. (1)) and the energy conservation relation (Eq. (2)). For the operating point data above, these may be computed to be:

$$\frac{\partial \phi}{\partial t} = -16.0 \text{ rad/cm}$$

$$\frac{\partial \phi}{\partial s} = -20.2 \text{ rad/cm}$$

$$\frac{\partial t}{\partial s} = -1.26$$

$$\left.\frac{\partial V}{\partial t}\right|_{ss} = -0.45 \text{ 1/sec}$$

$$\left.\frac{\partial V}{\partial s}\right|_{ss} = 0.56 \text{ 1/sec}$$

$$\frac{\partial V_g}{\partial s} = 0.19 \text{ 1/sec}$$

From these the system natural frequency and damping ratio may be calculated:

$$\omega_n = 0.75 \text{ rad/sec (frequency = .12 Hz)}$$

$$\xi = 0.8$$

In examining such frequency response data, there are several points of special interest. The first is the response of the system at low frequencies which essentially tests the steady-state aspects of the model and is not strongly related to the dynamics of the system. The high frequency response, on the other hand, provides essential information on the system dynamics. Of interest are the decay rate of the response amplitude with frequency and the maximum phase shift as they relate directly to the order of the system. If a system is second order, and the forcing function, or right hand side of the equation involves no derivatives of the input variable, the amplitude will decay as $1/\omega^2$ (-2 decades/decade) for high frequencies, and the phase angle will tend toward -180°. The response of thickness to pulling speed is such a case. These high frequency results may be obtained by substituting a constant times a sinusoid for both input and output and noting that at high frequencies the second derivative term dominates the left hand side of the equation. For a system with a first derivative of the input in the forcing function (as is the case with meniscus response) the high frequency response should fall off as $1/\omega$ (-1 decade/decade), and the phase angle should tend toward -90°. The final region of interest is that around the natural frequency. In a system with no derivative in the forcing function (e.g., thickness response), the natural frequency may be found by extending the high frequency data asymptote back up to the steady-state value of the response. This intersection, or break point, occurs at the natural frequency. The amount by which the response curve falls above or below the break point is indicative of the damping of the system. The further the curve falls below the break point, the higher the damping ratio.

As may be readily seen from Figs. 6 and 7, the data is in excellent agreement with the theory. Both steady-state values are close to those predicted by the theory. In the high frequency regions, the response magnitudes fall off precisely as expected: as a second-order system for thickness, and a first-order system for meniscus height response. In addition, the phase angle for meniscus height response tends toward -90° as expected, further verifying the order of the system. Further, the thickness response shows that the measured natural frequency is extremely close to the theoretical natural frequency. Finally, the thickness response curve indicates that the system has a damping ratio of approximately 1.2, slightly higher than the predicted value of 0.8.

In summary, we may say that the linearized formulation of the dynamics of the EFG process is quite accurate and does not deviate from the true actual dynamics in any important regard.

DIE TEMPERATURE RESPONSE TO CHANGES IN DIE HEATER POWER LEVEL

The dynamics of the die-heater thermal system are basically due to the thermal capacitances of the heater and the die. Accordingly, a lumped parameter thermal model has been formulated for this system as shown in Fig. 8.

Capacitor C_1 models the thermal capacitance of the die heater, while C_2 models the capacitance of the die itself. Resistor R_1 models the radiative and convective heat loss from the die heater to the environment. R_3 models the heat loss from the die to the environment, while R_2 models the thermal coupling between the die heater and the die. The heat source Q models the resistive power dissipation in the die heater.

As this lumped parameter system has two energy storage elements (two capacitors), it is a second-order system. The following second-order differential equations relate the die temperature T_d to the heat input Q.

$$\ddot{T}_d + 2\xi_t \omega_{n_t} \dot{T}_d + \omega_{n_t}^2 T_d = \left.\frac{\partial T_d}{\partial Q}\right|_{ss} \omega_{n_t}^2 Q, \qquad (15)$$

where $$\omega_{n_t}^{\ 2} = \frac{R_1 + R_2 + R_3}{R_1 R_2 R_3 C_1 C_2} \tag{16}$$

$$2\xi_t \ \omega_{n_t} = \frac{R_1 R_3 \ (C_1 + C_2) + R_2 \ (R_1 C_1 + R_3 C_2)}{R_1 R_2 R_3 C_1 C_2} \tag{17}$$

The capacitances may be calculated based on the volume of the die and heater and the specific heat of graphite. The resistances may be calculated by linearizing the heat loss mechanisms around the operating point temperature. If this is done, the following parameters may be calculated:

$$\omega_{n_t} = 0.35 \quad \text{rad/sec}$$

$$\xi_t = 1.7$$

$$\left.\frac{\partial T_d}{\partial Q}\right|_{ss} = 0.075 \ ^{o}\text{K/watt}$$

The magnitude and phase angle responses predicted by Eq. (15) are plotted in Fig. 9 along with the measured data. The experital value plotted at .001 Hz was obtained from the response to a step change input, as this frequency is sufficiently low so that the response may be approximated by the steady-state value. As can be seen, the measured low frequency, or steady-state value, for the response amplitude is close to the theoretical value. The behavior of the amplitude response at high frequencies is close to that predicted by the model; however, the model does not appear to predict quite a fast enough decay of amplitude with frequency. In fact, the decay rate of the data lies midway between what one would expect for a second and a third order system. However, the phase angle relationship behaves more like a second-order system, passing through -90° at the natural frequency of the system, and approaching -180° for high frequencies. Finally, note that the theory appears to accurately predict the natural frequency.

While the discrepancy between the measured and predicted amplitude response at high frequencies is not understood, the general agreement of the theory with experiment indicates that the model chosen is reasonable.

RIBBON THICKNESS AND MENISCUS HEIGHT RESPONSE TO CHANGES IN DIE HEATER POWER LEVEL

As discussed previously, it has been assumed that the complete system may be broken down into the separate and independent die heater thermal system and EFG system. If such were the case, we would expect the sinusoidal response amplitude of meniscus height to heater power to be given by the product of the response of the meniscus to die temperature and the response of die temperature to heater power. Thus,

$$\frac{|s|}{|Q|} = \frac{|s|}{|T_d|} \frac{|T_d|}{|Q|}$$

As may be seen from Eq. (8) and (9), the response of ribbon thickness and meniscus height to die temperature T_d is governed by the same physics as is the response to pulling speed. The only change is the addition of $\frac{\partial V_g}{\partial T_d}$ as a multiplicative constant on the right hand side of the equations. Thus, we may write:

$$\frac{|s|}{|Q|} = \frac{-\partial V_g}{\partial T_d} \frac{|s|}{|V|} \frac{|T_d|}{|Q|}$$

However, $\frac{\partial V_g}{\partial T_d}$ is difficult to obtain accurately from the steady-state theory. Thus, we cannot expect to be able to verify the theory at steady state, but should only be concerned with comparing the dynamics given by theory with experiment. We will, therefore, normalize the theoretical meniscus response to speed and the die temperature response to power by their respective theoretical steady-state values. In addition, we will use the measured steady-state value for meniscus response to power input. Thus:

$$\frac{|s|}{|Q|} = \frac{\frac{|s|}{|V|}}{\left.\frac{\partial s}{\partial V}\right|_{ss}} \frac{\frac{|T_d|}{|Q|}}{\left.\frac{\partial T_d}{\partial Q}\right|_{ss}} \left.\frac{\partial s}{\partial Q}\right|_{ss} \tag{18}$$

Similarly, we may write:

$$\frac{|t|}{|Q|} = \frac{\frac{|t|}{|V|}}{\left.\frac{\partial t}{\partial V}\right|_{ss}} \frac{\frac{|T_d|}{|Q|}}{\left.\frac{\partial T_d}{\partial Q}\right|_{ss}} \left.\frac{\partial t}{\partial Q}\right|_{ss}$$

Finally, we must expect that the phase angle of the meniscus response to input power should be the sum of the phase angles of the component responses:

phase angle meniscus to power	=	phase angle die temp. to power	+	phase angle meniscus to speed	

Figures 10 and 11 present the theoretical results as outlined above along with the experimental results. Again, the general agreement is apparent. In the case of the response of ribbon thickness, the theory indicates that we are multiplying two second-order systems together. We must, therefore, expect a fourth-order drop-off of amplitude with frequency, or a factor of 16 decrease for a doubling of the frequency in the high frequency region. The fact that the drop-off is so fast makes it extremely difficult to precisely determine the order of the system from the data. In fact, the high frequency data of Fig. 10 falls off at a rate between a fourth and fifth order system.

In the case of meniscus height response to power input, the theory indicates that we are multiplying two second-order systems, with one having a first derivative in the forcing function. Again, the drop-off rate at high frequencies is in good agreement with the theoretical value of -3 decades/decade (or an eight-fold decrease for a doubling of the frequency). Most notably, the measured phase angle does indeed tend toward -270°C at high frequencies as expected for a system with a third-order drop-off.

In summary, it seems that the complete heater-die-EFG system may indeed be separated into two distinct dynamic components and analyzed as such.

CONCLUSIONS AND IMPLICATIONS FOR CONTROL

Two basic types of systems that might be used to control

meniscus height have been discussed. In examining the elements of such controllers, the basic EFG system has been divided into two separate and distinct parts: the heater-die thermal system and the EFG system itself. The previously developed physical theory of the EFG growth process has been reviewed and extended so that it might be easily interpreted in the light of experimental data on dynamics. Further thermal system modeling is presented for the heater-die thermal system.

Experiments have been carried out on an instrumented crystal growth furnace on the two separate systems and the composite system as outlined above. In all cases, the agreement between theory and experiment has been found to be good. At low frequencies, the theoretical response amplitudes are in good agreement with the measured values, where applicable. This serves to establish the validity of the steady-state models. At high frequencies, the agreement is again good between theory and experiment, thus verifying that the system is of the order predicted by theory. Where measured, the phase angle data also indicates that the theory predicts the proper system orders. Finally, the theory is found to be in good agreement with the data as to the location of the system natural frequencies.

The results of this dynamic analysis may now be used to analyze a complete meniscus height control system. The results of these dynamic investigations show that meniscus height responds to die heater power level as a fourth-order system with a first-order derivative in the forcing function. In control engineers' parlance, the transfer function has four poles and one zero. Thus, if our meniscus height controller is to be die heater actuated, it must be able to accommodate the dynamic complexities of such a system. By starting with different types of control electronics (e.g., proportional, proportional plus integral, proportional plus derivative, various compensations, etc.), the composite system may be analyzed. For example, if simple proportional controlling action is assumed, it may be shown that the system is stable only for low values of the gain. Low gain values result in poor transient response and large steady-state

error of the output. In fact, such a control system was implemented and the system was indeed found to become unstable at approximately the gain predicted. Other controlling actions may be chosen for this system which represent a better compromise between stability, transient response, and steady-state error. However, under no circumstances is this an easy system to control. This is especially true when we realize that the operating point, and hence the dynamic behavior, of the system changes all the time, and the control system must be stable throughout the range of values encountered.

The difficulty of controlling this system stems from the fact that we are attempting to control meniscus height through a complex chain of dynamic events from just the final output, the meniscus height itself. In the traditional method of controlling meniscus height, two inputs are used; one from the die temperature, and the other from the perceived meniscus height. Since the die temperature is a system variable closer to the point of actuation, it serves to stabilize the system.

This same type of controller may be implemented automatically by deriving information from both the measured die temperature and meniscus height, rather than from meniscus height alone. However, another alternative exists. As the results of this study show, the meniscus height responds to pulling speed as a second-order system with a first-order derivative in the forcing function. In other words, the transfer function has two poles and one zero. Thus, we may build a much more straightforward meniscus height controller based on pulling speed actuation. In fact, it may be shown that a simple proportional controller based on pulling speed actuation will be stable for all values of the gain. Such a control system would allow the attainment of a high degree of stability, good transient response, and good steady-state behavior. It might further prove desirable to modulate both pulling speed and die heater power. The pulling speed would be used to control the system dynamics, while the die heater power would be used to compensate for long-term drifting which would otherwise carry the system out of the allowable speed range.

REFERENCES

[1] T. Surek, B. Chalmers, "The Direction of Growth of the Surface of a Crystal in Contact with its Melt," J. Crystal Growth 29 (1975) 1.

[2] E.M. Sachs, "Thermal Sensitivity and Stability of EFG Silicon Ribbon Growth," to be published in J. Crystal Growth.

[3] T. Surek, B. Chalmers and A.I. Mlavsky, J. Crystal Growth, 42 (1977) 453.

[4] E. Sachs, "In-Situ Carbon-Silicon Ribbon Thermocouple," to be published in J. Crystal Growth.

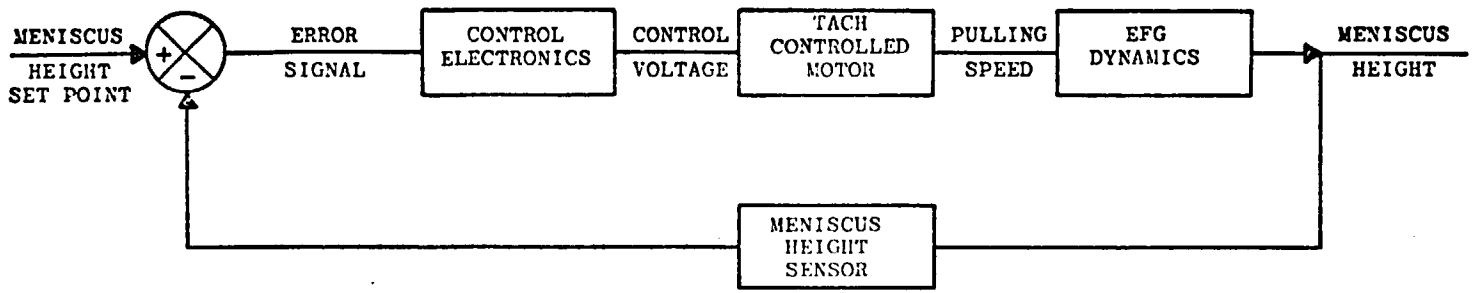

Fig. 1(a). Closed loop, pulling speed actuated meniscus height control system.

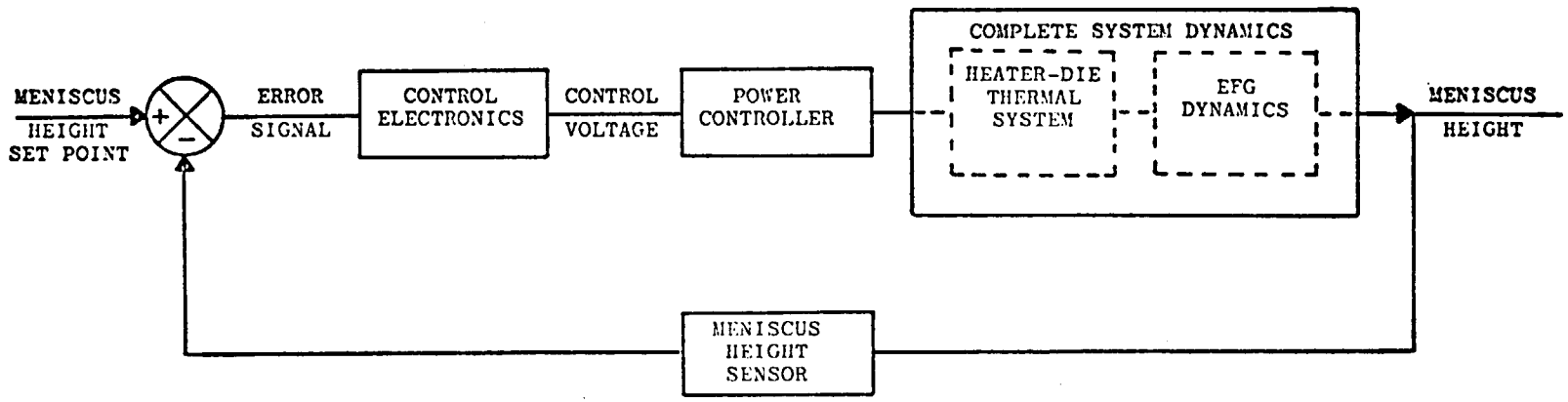

Fig. 1(b). Closed loop, die heater actuated meniscus height control system.

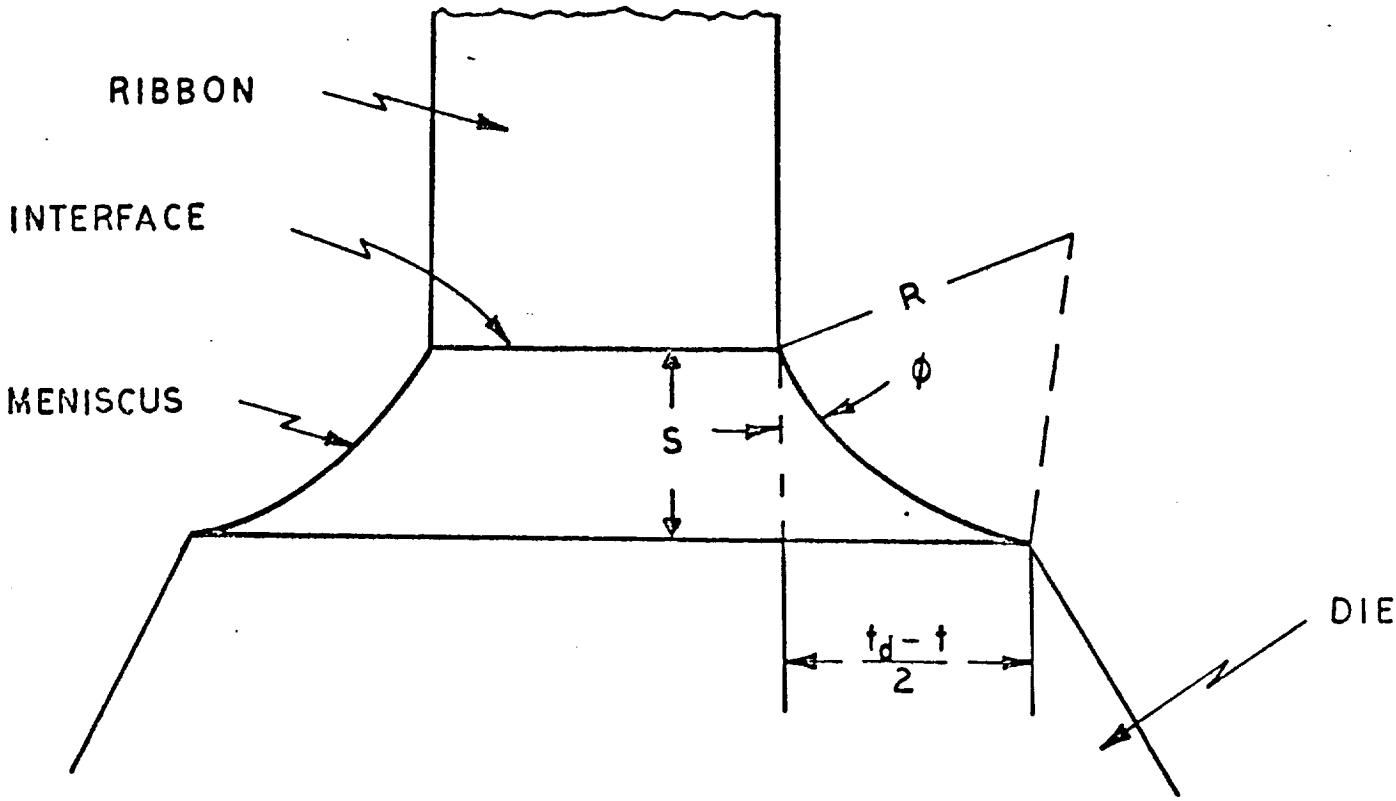

Fig. 2. Schematic view of meniscus shaping geometry in EFG.

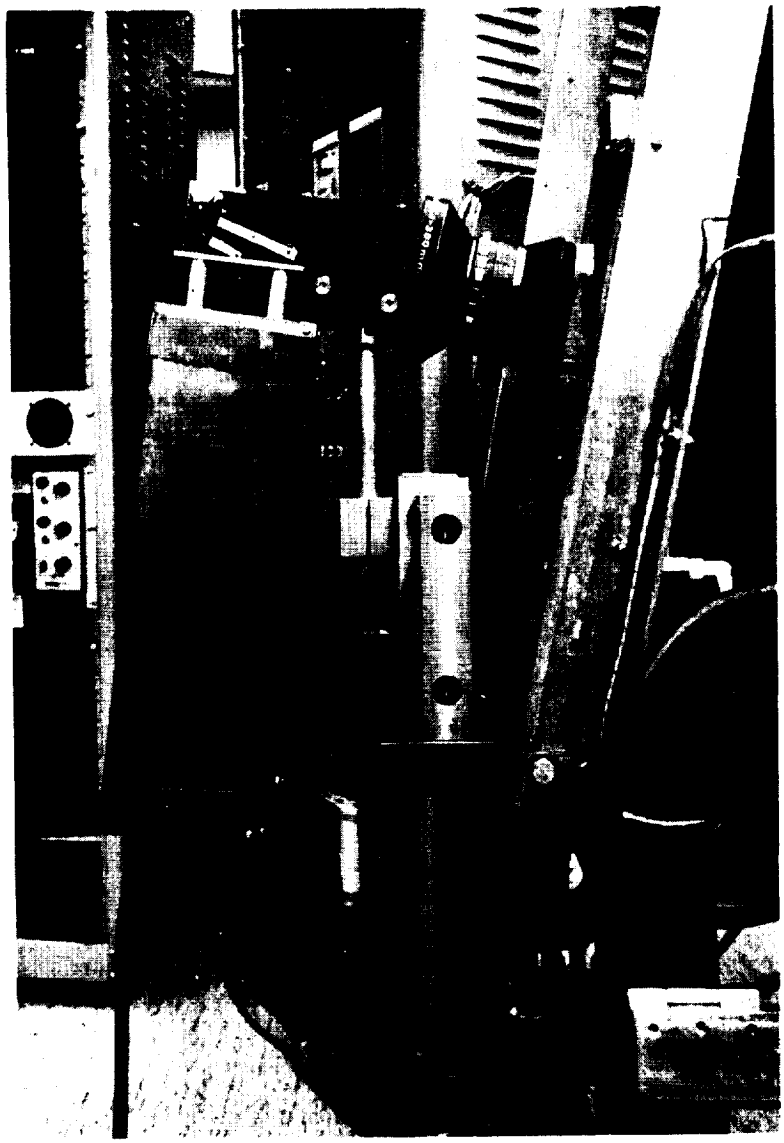

Fig. 3. Anamorphic optical-video system on instrumental crystal growth furnace.

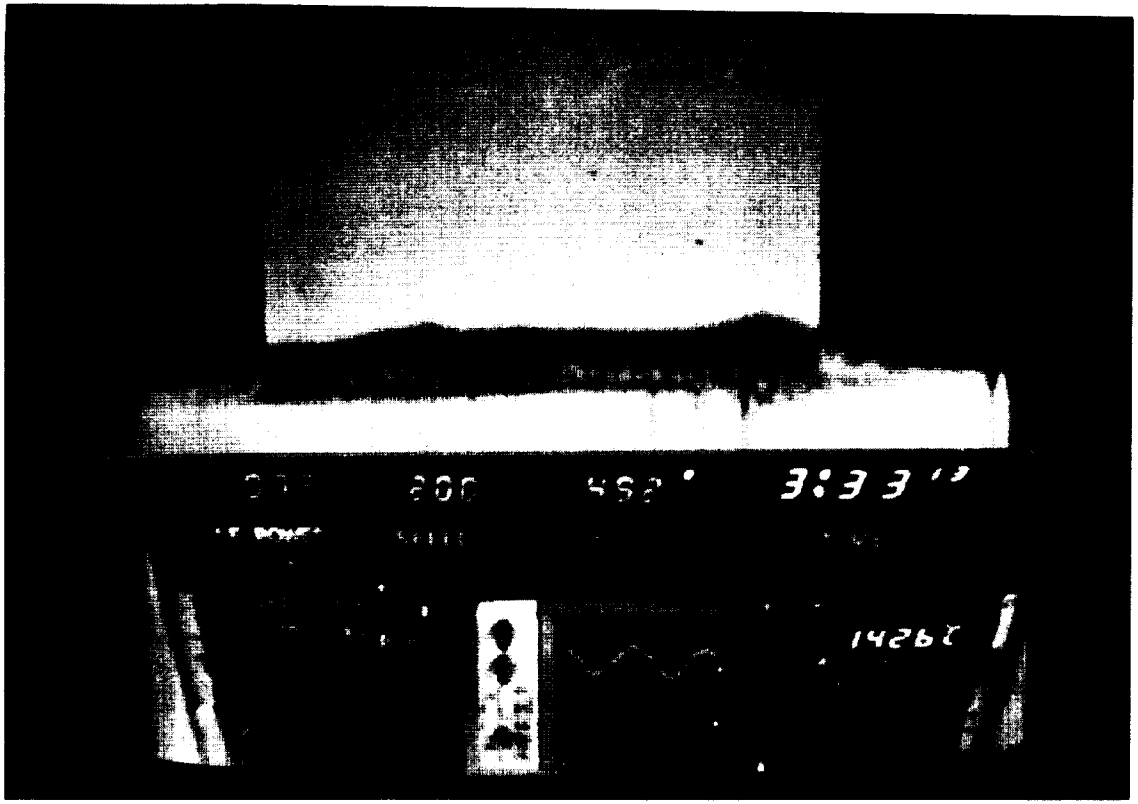

Fig. 4. Photograph of television monitor showing split screened image of ribbon growth and instrumentation.

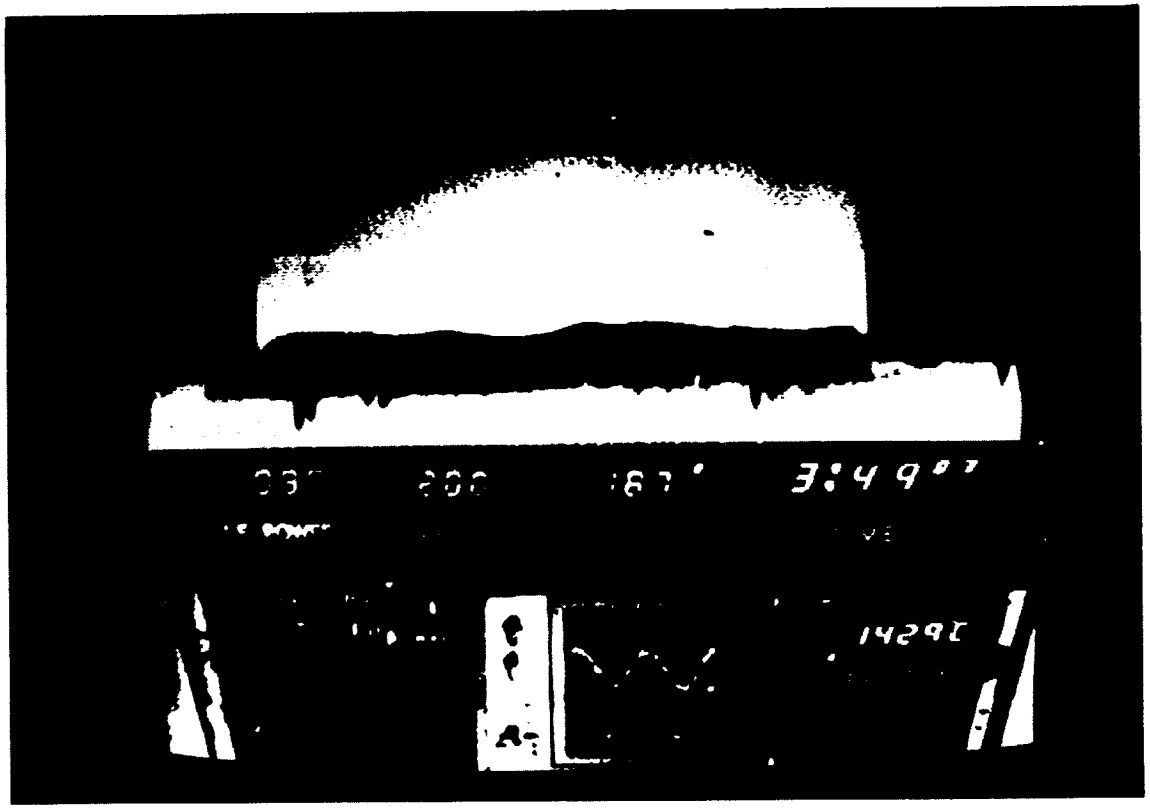

Fig. 5. Photograph of television monitor showing video processing of image of growth.

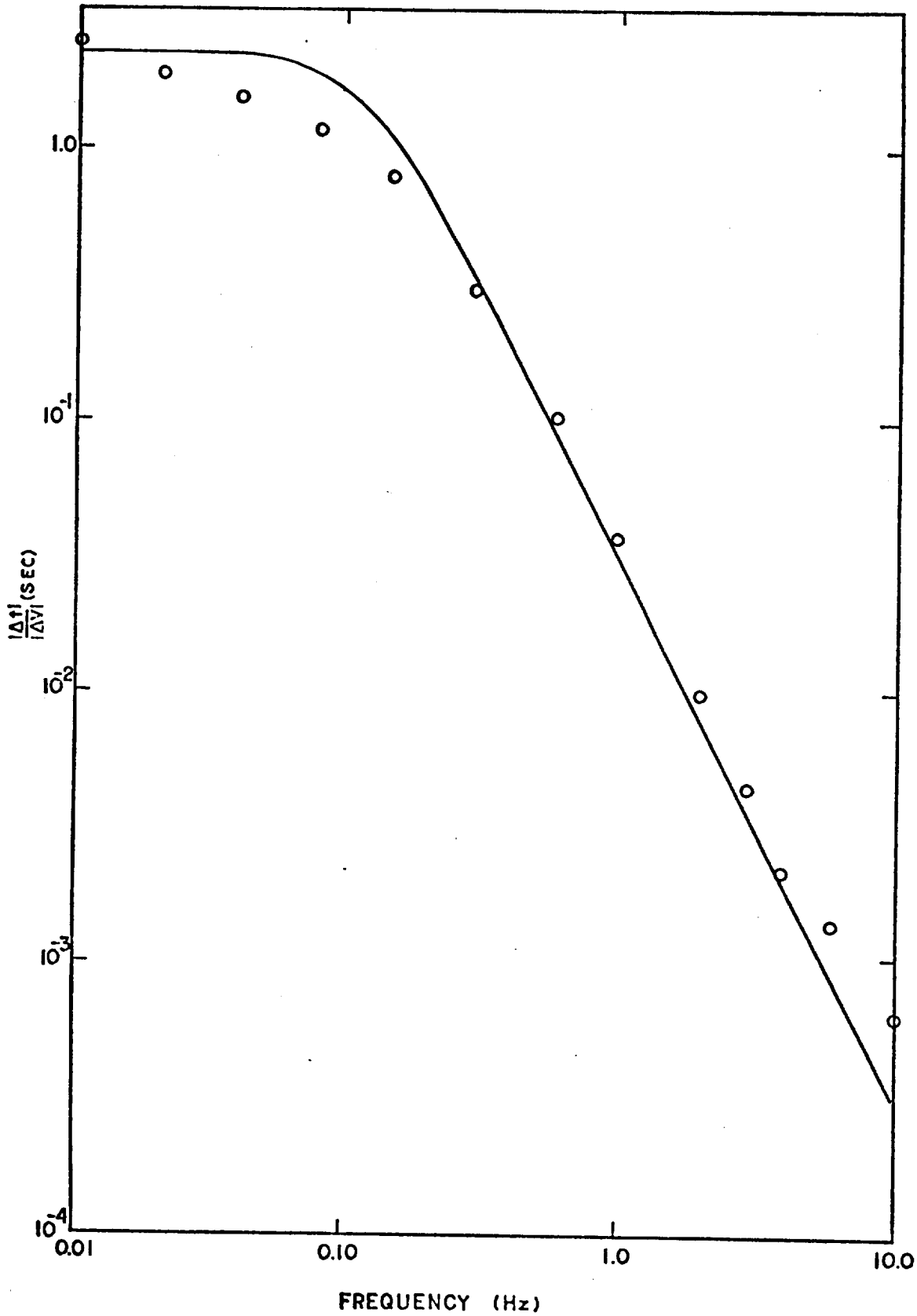

Fig. 6. Log-log frequency response plot showing the magnitude response of ribbon thickness to pulling speed.

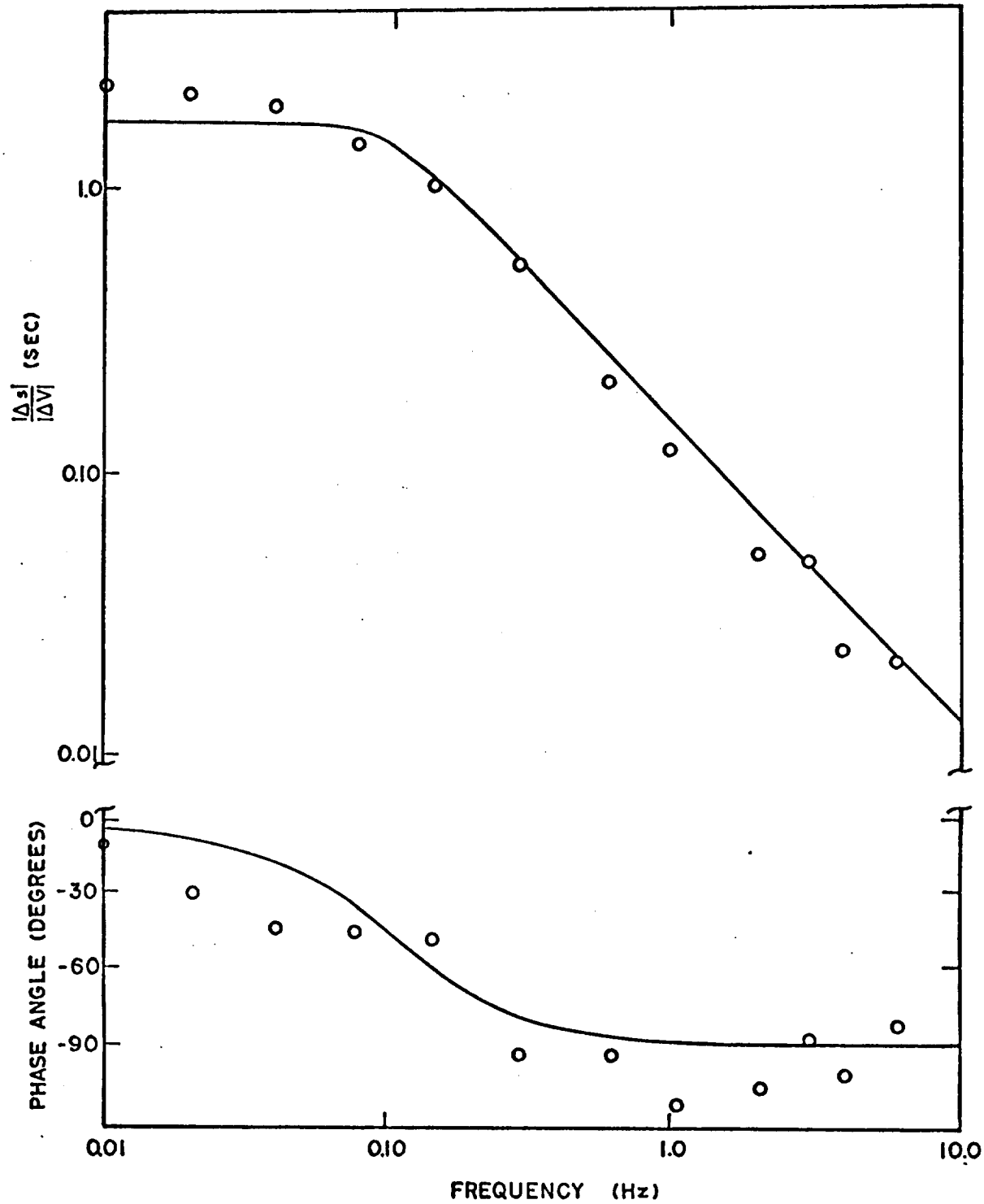

Fig. 7. Frequency response plot showing the magnitude and phase angle response of meniscus height, s, to pulling speed, V.

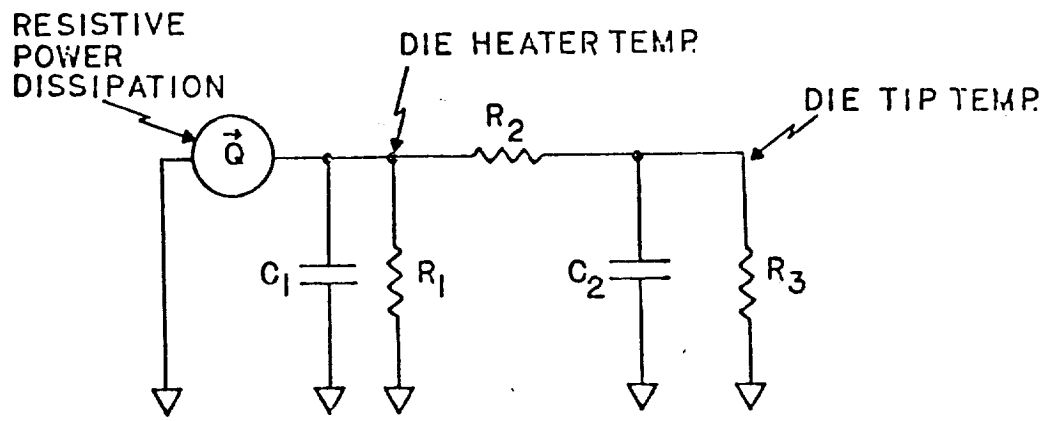

Fig. 8. Lumped parameter thermal model of the die-heater thermal system.

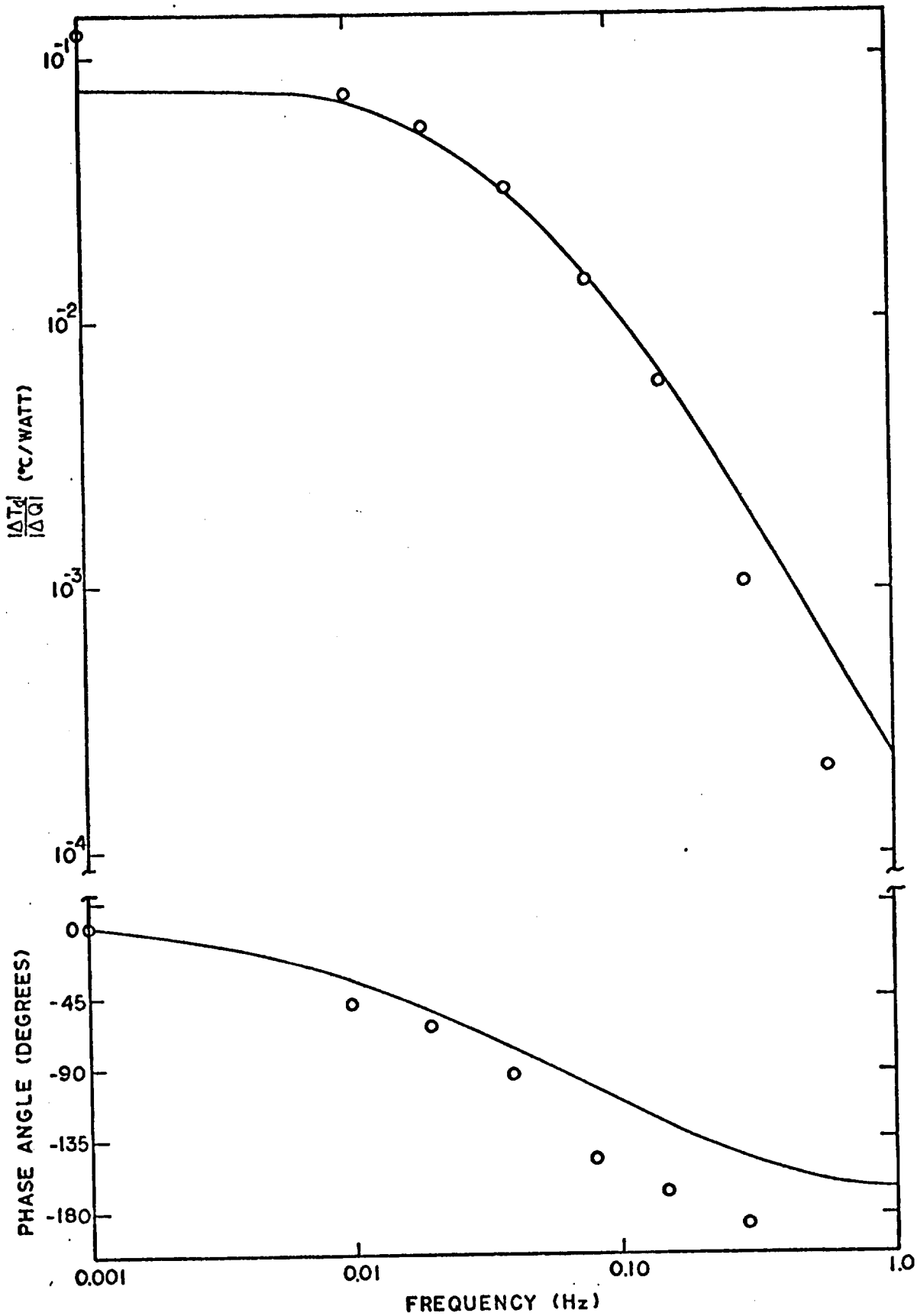

Fig. 9. Frequency response plot showing the magnitude and phase angle response of die temperature, T_d, to heater power level, Q.

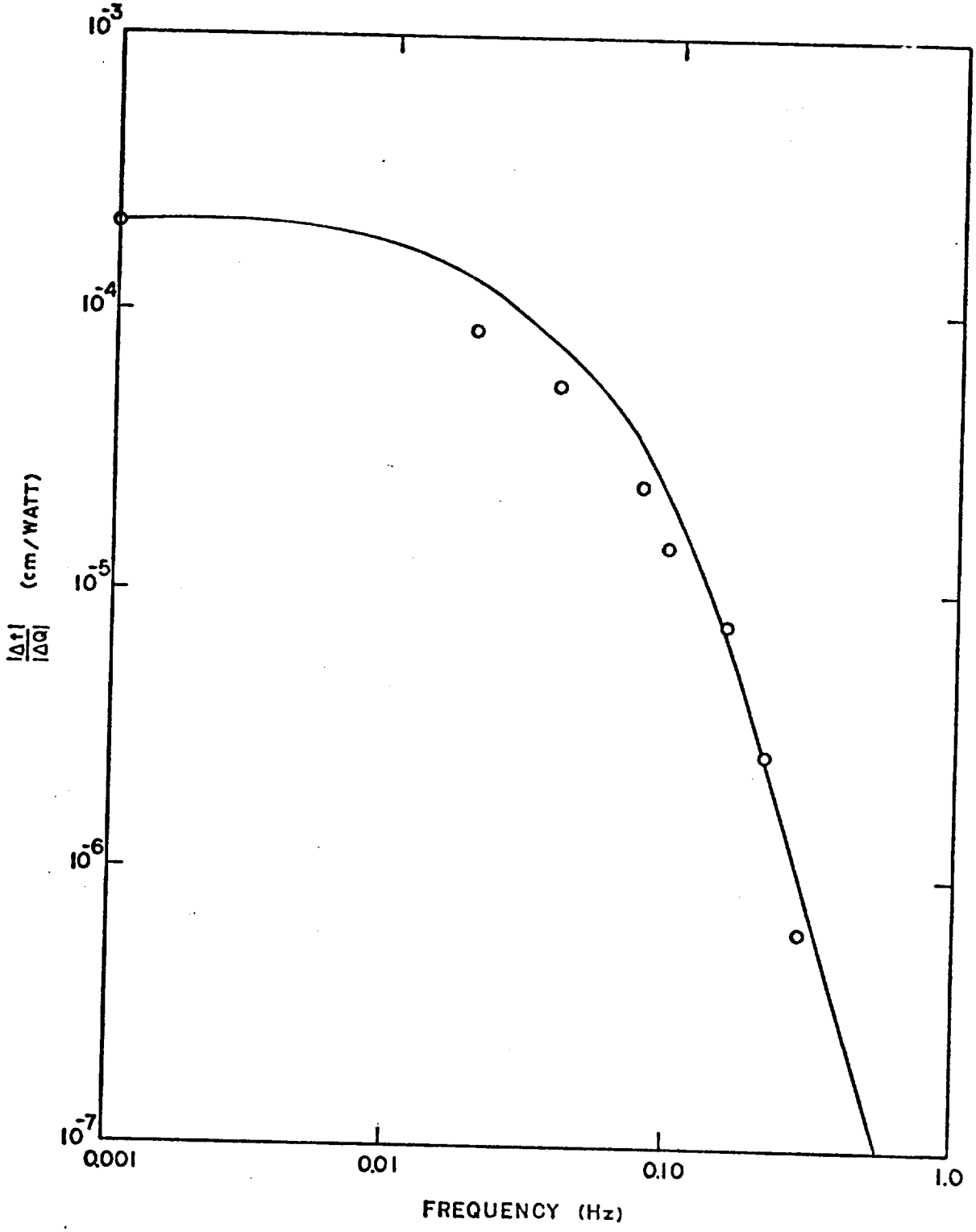

Fig. 10. Frequency response plot showing the magnitude response of ribbon thickness, t, to heater power level, Q.

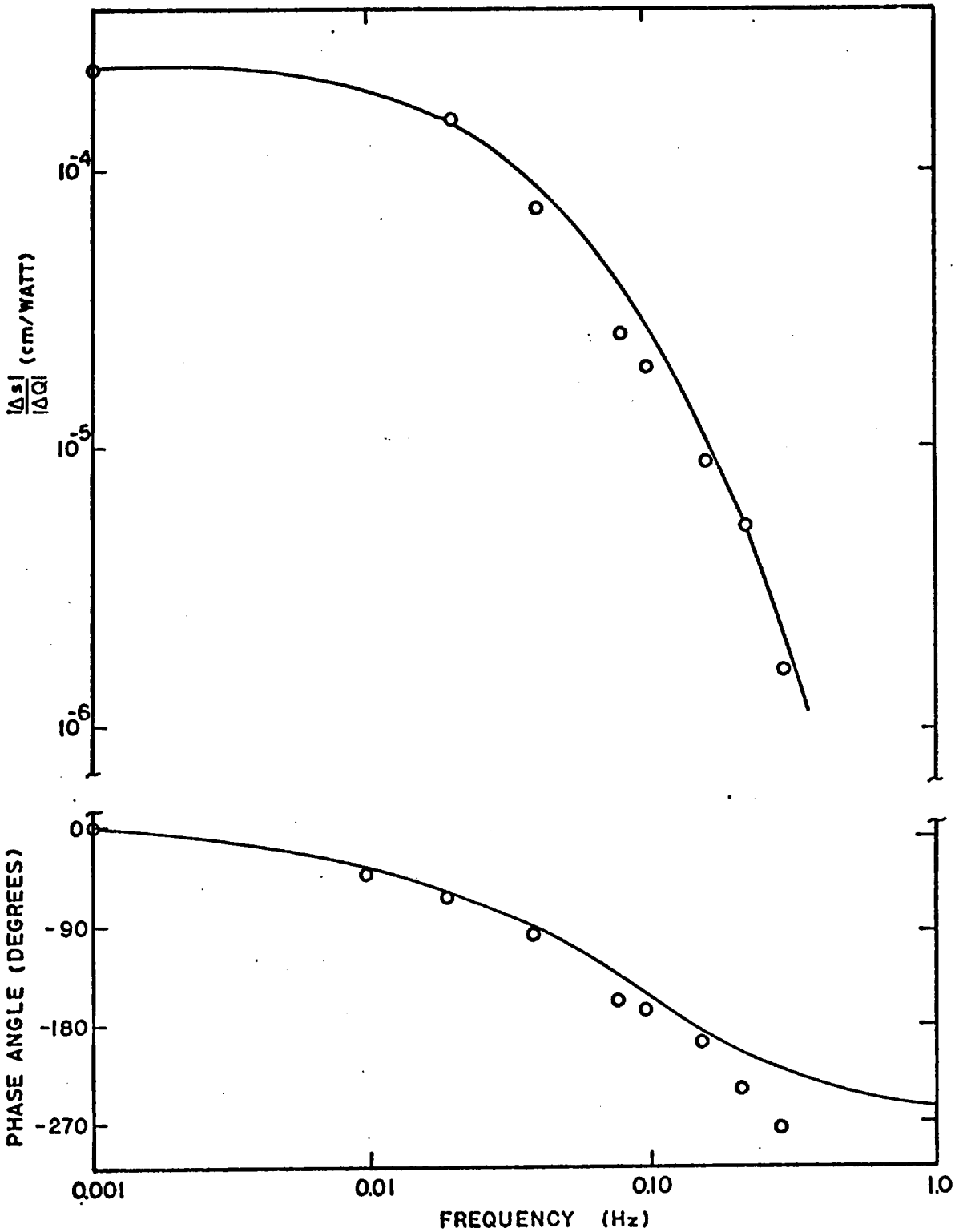

Fig. 11. Frequency response plot showing the magnitude and phase angle response of meniscus height, s, to heater power level, Q.